European Commission

JRC TECHNICAL REPORT

Assessment of Copernicus OLCI Ocean Colour Data

Zibordi G., Talone M., Mélin F., Sciuto P.,
Berthon J.-F., Bulgarelli B. and Canuti E.

2019

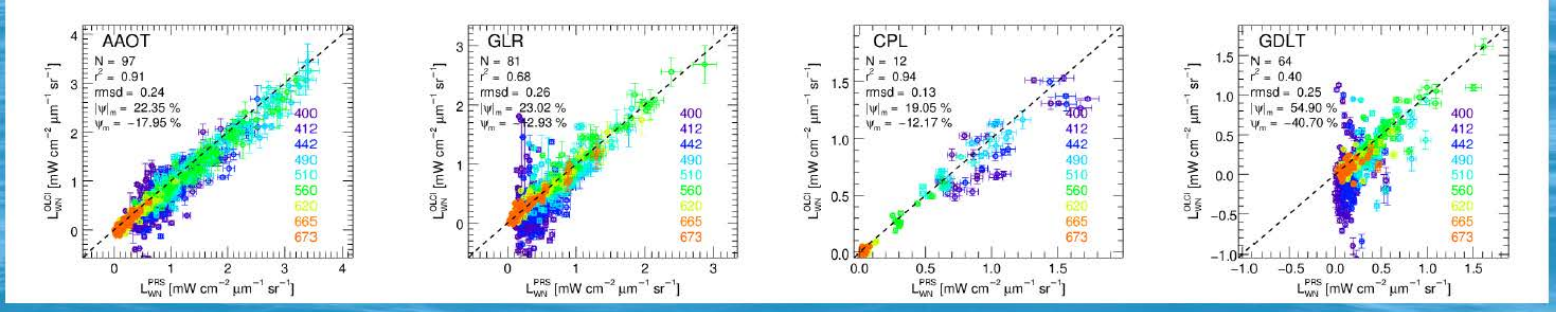

Joint Research Centre

EUR 29973 EN

Contact information
Name: Giuseppe Zibordi
Address: Via E. Fermi 2749
Email: giuseppe.zibordi@ec.europa.eu
Tel.: +39 0332 785902

EU Science Hub
https://ec.europa.eu/jrc

JRC118718

EUR 29973 EN

PDF	ISBN 978-92-76-13039-0	ISSN 1831-9424	doi:10.2760/41229
Print	ISBN 978-92-76-13038-3	ISSN 1018-5593	doi:10.2760/185842

Luxembourg: Publications Office of the European Union, 2019

How to cite this report: Zibordi G., Talone M., Mélin F., Sciuto P., Berthon J.-F., Bulgarelli B. and Canuti E., *Assessment of Copernicus OLCI Ocean Colour Data*, EUR 29973 EN, Publications Office of the European Union, Luxembourg, 2019, ISBN 978-92-76-13039-0, doi:10.2760/41229, JRC118718.

Contents

Acknowledgements

This work is a contribution to *i. Earth Observation Support to Copernicus Climate and Marine Services* (EOSS) funded by the Directorate-General Joint Research Centre (JRC) and to *ii. Reference In Situ Data for Calibration and Validation* part of the Administrative Arrangement on Copernicus between the Directorate-General for Internal Market, Industry, Entrepreneurship and SMEs (DG GROW) and JRC.

Authors

Giuseppe Zibordi, Marco Talone, Frédéric Mélin, Pietro Sciuto, Jean-François Berthon, Barbara Bulgarelli and Elisabetta Canuti.

Abstract

The Copernicus Program has been established through the Regulation EU No377/2014 with the objective to ensure long-term and sustained provision of accurate and reliable data on environment and security through dedicated services. Among these, the Copernicus Marine Environment Monitoring Service and the marine component of the Climate Change Service, both rely on satellite ocean colour observations delivering data on water quality and climate relevant quantities such as chlorophyll-a concentration used as a proxy for phytoplankton biomass.

This report summarizes results from activities carried out at the Joint Research Centre (JRC) to assess Copernicus Sentinel-3A and Sentinel-3B Ocean Land Colour Instrument (OLCI) radiometric data products in view of ensuring their confident use in environmental and climate applications.

1 Introduction

The spectral normalized water-leaving radiance L_{WN} or alternatively the equivalent remote sensing reflectance R_{RS}, indicate the light emerging from the sea retrieved from the top of the atmosphere radiance detected by a satellite ocean colour sensor [see Zibordi et al. 2014]. Spectral values of L_{WN} and R_{RS} are then the primary ocean colour data products applied to determine geophysical quantities such as the near-surface chlorophyll-a concentration (*Chla*) used as a proxy for phytoplankton biomass. Consequently, the accuracy of derived quantities primarily depends on the accuracy of primary radiometric products.

The assessment of L_{WN} is thus a fundamental need for any satellite ocean colour mission to verify the capability to meet uncertainty requirements: i.e., 5% for L_{WN} in the blue-green spectral regions in view of determining *Chla* with an uncertainty better than 35% in oceanic waters.

Figure 1 illustrates the complexity of the ocean colour paradigm that, in addition to satellite data, requires a number of basic components spanning from field reference measurements, radiative transfer and bio-optical modelling and advanced methods for time series analysis.

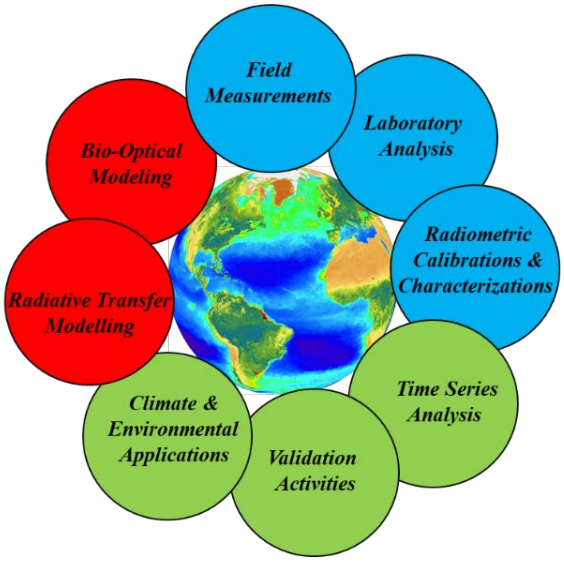

Figure 1. Schematic illustrating the various activities contributing to the development, assessment and exploitation of satellite ocean colour data.

Within such a general context, this report summarizes results from activities carried out at the Joint Research Centre (JRC) to assess Copernicus ocean colour Ocean Land Colour Instrument (OLCI) data products in view of ensuring their confident use in environmental and climate applications. Specifically, the report summarizes results from the validation of OLCI radiometric data products across European Seas. The analysis focusses on reduced resolution (RR) data from OLCI operated on-board Sentinel-3A (i.e., OLCI-A) since February 2016, and onboard Sentinel-3B (i.e., OLCI-B) since April 2018.

The overall objective is to provide an updated assessment of the accuracy of Level-2 ocean colour Non-Time Critical (NTC) radiometric products from the Operational Processing Baseline 2.23 applied to OLCI 1.2 km resolution data [EUMETSAT 2018a, 2018b]. OLCI data were downloaded from the Copernicus Online Data Access Reprocessed (CODAREP) dataset containing S3A data up to November 2017. Subsequent data, defined as “operational” were downloaded from the EUMETSAT Data Centre (https://www.eumetsat.int/website/home/Data/DataDelivery/EUMETSATDataCentre/index.html).

2 AERONET-OC

The validation of OLCI-A and OLCI-B ocean colour radiometry data products largely rely on the Ocean Colour component of the Aerosol Robotic Network (AERONET-OC). AERONET [Holben *et al.* 1998] is a federated instrument network and data archive managed by the Goddard Space Flight Center (GSFC) of the U.S. National Aeronautics and Space Administration (NASA) specifically conceived to support aerosol investigations through standardized instruments and methods [Holben *et al.* 2001]. Similar to AERONET, its Ocean Color component [AERONET-OC, Zibordi *et al*. 2009] relies on NASA's commitment for field instruments calibration, data processing and archiving, complemented by the JRC involvement in the continuous revision of processing algorithms and quality control of data products. These activities are accompanied by independent actions focused on establishing and maintaining CE-318 dedicated sun-photometers at coastal sites of interest for individual investigators or research institutions. These sun-photometers, called SeaWiFS Photometer Revision for Incident Surface Measurements (SeaPRISM), have the capability of performing autonomous above−water radiometric measurements in addition to the more common atmospheric measurements.

Key features of AERONET-OC are: *i.* near-real time data collection and processing (i.e., within a few hours); *ii.* use of a standardized instrument, calibration procedure and data processing; *iii.* open access to measurements and products. The primary data product of AERONET-OC is the normalized water-leaving radiance L_{WN} at wavelengths suitable for satellite ocean color applications. An additional product is the aerosol optical thickness, τ_a, complemented by phase function, particle size distribution and single scattering albedo of aerosols, all having potential importance to assess the performance of the atmospheric correction process applied to satellite data.

AERONET-OC L_{WN} data products undergo extended quality controls which include checking for: *i.* cloud contamination; *ii.* high variance of multiple sea- and sky-radiance measurements utilized for computing L_{WN}; *iii*. elevated differences between pre- and post-calibrations of SeaPRISM sun-photometers; and *iv*. spectral inconsistency of L_{WN} data. Estimated relative uncertainties of *in situ* L_{WN} data are 4-5% in the blue-green spectral regions and ~8% in the red for moderately turbid waters [Zibordi et al. 2009]. Relative uncertainties may increase at sites exhibiting very low L_{WN} values such as those obtained in the extremely absorbing waters of the Baltic Sea, [Gergely and Zibordi 2014]. These uncertainties have been quantified accounting for contributions from: *i.* absolute calibration; *ii.* change in instrument sensitivity during each deployment period; *iii.* corrections for the off-nadir viewing geometry and the anisotropy of the seawater light field; *iv.* variability in specific parameters required for the determination of L_{WN} (e.g., wind speed, surface reflectance, diffuse atmospheric transmittance); and finally, *v.* environmental perturbations (e.g., wave effects, changes in illumination and seawater optical properties during measurements).

2.1 Measurement sites

AERONET-OC deployment requirements for the collection of measurements suitable for ocean color validation activities are summarized as follows: *i.* fixed deployment platforms allowing for measurement of the direct sun irradiance through accurate sun-tracking; *ii.* superstructures with height and shape minimizing contamination of the measuring system by sea-spray; and *iii.* deployment positions allowing unobstructed sea observations at the maximum possible distance from the superstructure at the time of satellite overpass. Any AERONET-OC site should ideally be at a distance from the mainland allowing to assume that the adjacency effects are negligible in the remote sensing data. It is recalled that the adjacency

effects [Bulgarelli et al. 2014] are produced by the different reflectance of nearby surfaces, and the magnitude of the related perturbations in the remote sensing data is a function of the spectral reflectance of surfaces and of the optical properties of the atmosphere (mostly the aerosol type and load). As a rule of thumb, any distance greater than 5-10 nautical miles is considered suitable. A further requirement for ideal AERONET-OC sites, is a water depth sufficient to neglect the bottom effects. A simple scheme for quantifying these effects has been proposed by Zibordi et al. [2009] accounting for the seawater optical properties as defined through the diffuse attenuation coefficient K_d and the irradiance reflectance R.

Figure 2 shows the current location of the existing, planned and potential AERONET-OC sites. Table 1 provides basic detail for current sites (the JRC AERONET-OC sites are highlighted in blue).

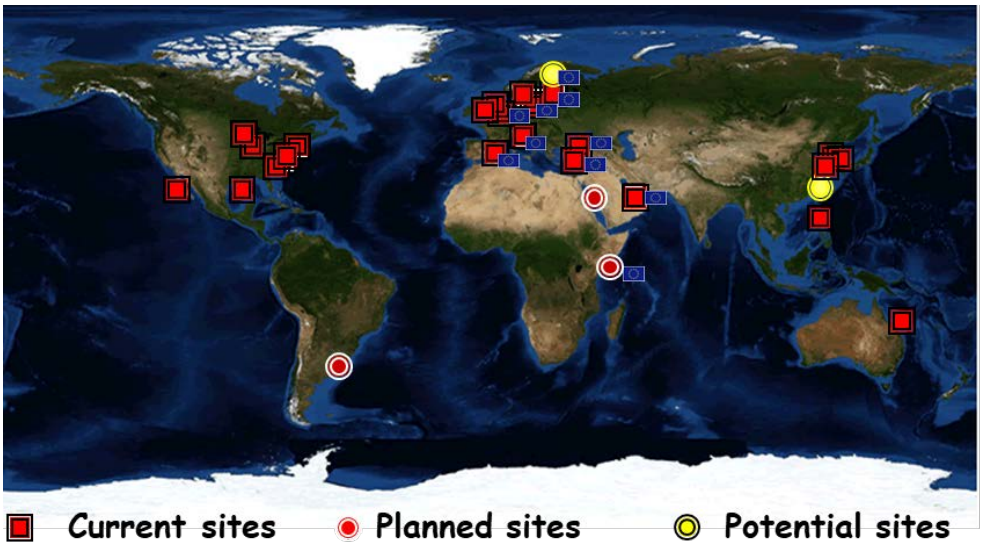

Figure 2. Current, planned and potential AERONET-OC sites. General information on current AERONET-OC sites is given in Table 1 (the sites maintained/planned by the JRC are highlighted through the EU flag).

The current operational JRC AERONET-OC sites (see Figure 3) specifically include:

1. The *Acqua Alta Oceanographic Tower* (AAOT, also called Venise) in the northern Adriatic Sea established and operated since 2002;
2. The *Gustaf Dalen Lighthouse Tower* (GDLT) in the Baltic Proper established and operated since 2005;
3. The *Helsinki Lighthouse Tower* (HLT) site in the Gulf of Finland established and operated since 2006;
4. The *Gloria* (GLR) platform in the north Western Black Sea established and operated since 2010;
5. The *Galata Platform* (GLT) in the south Western Black Sea established and operated since 2014.
6. The *Irbe Lighthouse* (ILT) in southern Gulf of Finland established and operated since 2018.
7. The *Casablanca Platform* (CPL) in Western Mediterranean Sea established and operated since 2019.
8. The *Section-7 Platform* (ST-7) in Western Black Sea established and operated since 2019 (this site replaces *Gloria* since August 2019).

Table 1. Current AERONET-OC sites. The years in brackets indicate the operation period. AAOT, GDLT, HLT, AABP, GLR, GLT, ILT, CPL and ST-7 are indicated as Venise, Gustav Dalen Tower, Helsinki Lighthouse, Abu-Al-Bukhoosh, Gloria, Galata, Casablanca and Sation-7 within the AERONET Ocean Color web page (http://aeronet.gsfc.nasa.gov). The AERONET-OC established and managed by the JRC are highlighted in blue.

Site	Region	Lat.	Lon.	Structure	Responsible Institutions
AAOT (2002-ongoing)	**Adriatic Sea**	**45.314°N**	**12.508°E**	**Oceanographic tower**	**Joint Research Centre (EU)**
MVCO (2004-ongoing)	Mid-Atlantic Bight	41.325°N	70.567°W	Oceanographic tower	University of New Hampshire (US)
GDLT (2005-ongoing)	**Baltic Proper**	**58.594°N**	**17.467°E**	**Lighthouse**	**Joint Research Centre (EU)**
COVE (2005-ongoing)	Mid-Atlantic Bight	36.900°N	75.710°W	Lighthouse	National Aeronautics and Space Administration (USA)
HLT (2006-ongoing)	**Gulf of Finland**	**59.949°N**	**24.926°E**	**Lighthouse**	**Joint Research Centre (EU)**
AABP (2006-2008)	**Persian Gulf**	**25.495°N**	**53.146°E**	**Oil platform**	**Joint Research Centre (EU)**
Palgrunden (2008-ongoing)	Palgrunden Lake	58.753°N	13.158°E	Lighthouse	University of Stockholm (S)
LUCINDA (2009-ongoing)	Coral Sea	18.519°S	146.385° E	Jetty	Commonwealth Scientific and Industrial Research Organisation
LISCO (2009-ongoing)	Long Island Sound	40.955°N	73.342°W	Platform	City College of New York (USA)
WaveCIS_Site_CSI_6 (2010-ongoing)	Gulf of Mexico	28.867°N	90.483°W	Oil platform	Louisiana State University (USA)
GLR (2010-ongoing)	**Western Black Sea**	**44.600°N**	**29.360°E**	**Gas platform**	**Joint Research Centre (EU)**
USC 2011-ongoing)	US Pacific Coast	33.564°N	118.118°W	Oil platform	University of Southern California (USA)
Gageocho (2011-2012)	Yellow Sea	33.942°N	124.593°E	Oceanographic tower	Korea Ocean Research & Development Institute (KR)
GOT (2012-2016)	Gulf of Thailand	09.285N	101.407 E	Oil platform	National Aeronautics and Space Administration (USA)
Ieodo 2013-ongoing	Yellow Sea	32.123°N	125.182°E	Oceanographic tower	Korea Ocean Research & Development Institute (KR)
GLT (2014-ongoing)	**Western Black Sea**	**43.045°N**	**28.193° E**	**Gas platform**	**Joint Research Centre (EU)**
Zeebrugge (2014-ongoing)	North Sea	51.362°N	3.120° E	Measuring platform	Management Unit of the North Sea Mathematical Models (BE)
Socheongcho (2015-ongoing)	Yellow Sea	37.423°N	124.738° E	Oceanographic Platform	Korea Ocean Research & Development Institute (KR)
Thornton_C-power (2015-ongoing)	North Sea	51.533°N	2.955° E	Measuring platform	Management Unit of the North Sea Mathematical Models (BE)
Blyth_NOAH (2016-ongoing)	North Sea	55.146° N	1.4209°	Lighthouse	University of Hull (UK)
Lake_Erie (2016-ongoing)	Lake Erie	41.826° N	83.194°° W	Lighthouse	University of New Hampshire
Ariake Tower (2018-ongoing)	Ariake Sea	33.104° N	130.272° E	Service Platform	Nagoya University
ILT	**Gulf of Finland**	**57.751°** N	**21.723°** E	**Lighthouse**	**Joint Research Centre (EU)**
Lake Okeechobee	Lake Okeechobee	26.902° N	80.789° W	Service platform	National Aeronautics and Space Administration (USA)
South Greenbay	Lake Michigan	44.596° N	87.951° W	Service platform	National Aeronautics and Space Administration (USA)
Grizzly Bay	Grizzly Bay	38.108° N	122.056° W	Service platform	National Aeronautics and Space Administration (USA)
CPL (2019-ongoing)	**Western Med Sea**	**40.717°** N	**1.358°** E	**Oil platform**	**Joint Research Centre (EU)**
ST-7 (2019-ongoing)	**Western Black Sea**	**44.546°** N	**29.447°** E	**Gas platform**	**Joint Research Centre (EU)**

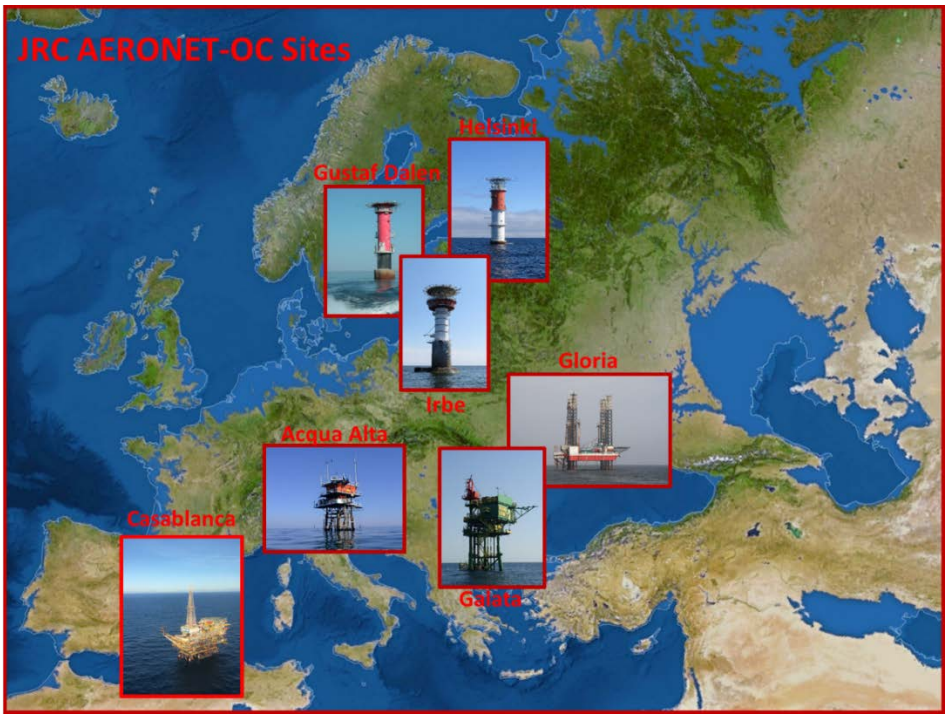

Figure 3. Locations and infrastructures of the JRC AERONET-OC sites.

2.2 Data handling and access

AERONET-OC makes full use of the existing AERONET data acquisition, processing, archiving, and distribution infrastructure [Holben *et al.* 1998]. Data acquisition mechanisms primarily include transmitters for relaying measurements to geostationary meteorological satellites (GOES, METEOSAT or GMS), internet or GPRS for direct transfer of data to the AERONET central infrastructure at GSFC. The latter data are then processes in near real-time along with ancillary data input (e.g., surface pressure and wind speed). Raw data and derived products at the various quality levels are stored in a specific database for each instrument on an hourly basis and are made publicly available through the AERONET web interface (https://aeronet.gsfc.nasa.gov) under a specified data policy (i.e., *Due to the research and development phase characterizing AERONET-Ocean Color, use of these data requires offering co-authorship to the Principal Investigator. Additionally, the original source of data, i.e., https://aeronet.gsfc.nasa.gov/new_web/ocean_color.html , needs to be acknowledged*). It is specified that the data policy is mostly intended to guard the integrity of data and avoid their misinterpretation and misapplication. This already happened despite of the rich literature detailing data processing and quality assurance/control steps.

The AERONET web site provides aerosol microphysical and optical property products (e.g., optical thickness, size distribution, phase function and single scattering albedo), together with L_{WN} data for each site. Product map browsers provide a geospatial perspective of the available AERONET data for each site. Web interfaces provide site information, data plots, and additionally support data download. Aerosol and ocean color derived products are displayed in daily, monthly, and yearly plots. Each data product may be browsed and downloaded by type, date, and quality level. Additional related Earth science data products, such as atmospheric and oceanic satellite retrievals and 7-day back-trajectory analysis products, are also available for most AERONET sites.

Fully quality-assured (i.e., Level 2.0) AERONET-OC data imply: (i) existence of complete measurement sequences including the total radiance from the sea $L_T(\lambda)$ and the sky-radiance $L_i(\lambda)$ collected with specific viewing geometry [Zibordi et al. 2009]; (ii) wind speed W<15 m s^{-1}; (iii) existence of cloud-screened level 2 AERONET $\tau_a(\lambda)$ data; (iv) exclusion of $L_{WN}(\lambda)$ spectra exhibiting negative values; (v) low variance in measurement sequences of $L_i(\lambda)$ indicating stable illumination conditions and of $L_T(\lambda)$ indicating small wave and foam perturbations; (vi) differences lower than 5% between pre- and post-deployment absolute radiometric calibration coefficients; (vii) self-consistency of the shape of $L_{WN}(\lambda)$ spectra; (viii) finally, exclusion of dubious data as a result of a spectrum-by-spectrum screening by an experienced scientist. These criteria lead to acceptance rates of Level-2 $L_{WN}(\lambda)$ data varying between a very few to a few ten percent [Zibordi et al. 2009]. The different rates are mostly due to site-specific factors like restrictions imposed by the instrument set-up, cloudiness or quality of data transmissions.

Metadata for AERONET-OC Level-2 data from sites maintained by the JRC, are accessible through the JRC Data Catalogue web client

https://data.jrc.ec.europa.eu/dataset?sort=sort_criteria+desc%2C+title_string+asc&projects=AERONET-OC .

2.3 Advances supporting OLCI validation

The AERONET-OC radiometers operated since 2002 have 9-channels largely centered on the Moderate Resolution Imaging Spectroradiometer (MODIS) center-wavelengths. That spectral configuration does not, however, support the simultaneous assessment of all the relevant OLCI radiometric data at the visible center-wavelengths. Because of this, with specific funding from DG-GROW (responsible for the Copernicus Space activities), and, in collaboration with NASA and the instrument manufacturer, a new version of the AERONET-OC system has been defined and included in the network. This new instrument, fully consistent with the previous one in terms of measurement performance, has an extended number of channels that allows the full assessment of the OLCI ocean color radiometry data in the visible spectral region. Also, in view of extending the AERONET-OC support to inland water applications, in addition to the 'sea' spectral configuration, a 'lake' one has been defined.

Table 2 shows the center-wavelengths of major satellite ocean color sensors and those of the various AERONET-OC spectral band settings

Table 2. Center-wavelengths of main ocean color sensors (i.e., MODIS, VIIRS and OLCI) compared to those of the AERONET-OC system (for both the 'sea' and 'lake' configurations).

Satellite Sensors	Wavelengths [nm]																					
MODIS		412.5	443	488		531	551			667	678		748				870		905	940		
VIIRS (20 nm)		412	445	488				555		672			746			865						
OLCI (10 nm)	400	412.5	442.5	490	510			560	620	665	681	709	754	...	779	865		885	900	940	1020	
AERONET-OC																						
PRS-09		412	443	488		531	551			667							870					
PRS-12 (sea)	400	412.5	442.5	490	510			560	620	665					779	865				940	1020	
PRS-12 (lake)		412.5	442.5	490	510			560	620	667	681	709				865				940	1020	

It is mentioned that the testing of the new AERONET-OC instruments implied a necessary upgrade of the capabilities of the JRC Marine Optical Laboratory to cope with new technical requirements. This specifically implied an expansion and adaptation of the Field Support Facility comprising in-lab and external infrastructures (see Fig. 4). Additionally, in view of cross-comparing data products from the 9- and 12-channel instruments and verify their full consistency, a special infrastructure has been realized at the AAOT (see Fig. 5). This is currently allowing for simultaneous measurements under identical observation conditions through 9- and 12-channel systems.

Figure 4. AERONET-OC Field Support Facility of the Marine Optical Laboratory comprising an in-lab (left panel) and external (right panel) infrastructures.

Figure 5. The AAOT site in the northern Adriatic Sea (left panel) and the dedicated AERONET-OC deployment structure (right panel) contemporaneously hosting 9- and 12-channel systems for data cross-comparison.

Inter-comparisons between water-leaving radiances L_W produced over a one-year deployment period at the AAOT with AERONET-OC 9- and 12-channel radiometers are presented in Fig. 6 at corresponding spectral bands. Results, definitively, confirm the equivalence of the two systems and their confident inter-changeability.

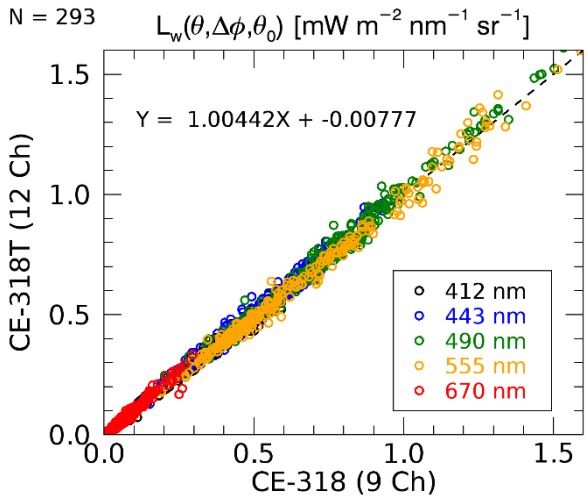

Figure 6. Inter-comparison of AERONET-OC water-leaving radiances L_W from measurements performed at the AAOT with the 9- and 12-channel radiometers. Data are presented at corresponding bands exhibiting center-wavelengths at, or nearby, 412, 443, 490, 555, and 670 nm.

3 Methods

Validation results presented here for OLCI-A and OLCI-B were obtained from matchups (i.e., quasi coincident *in situ* and satellite data) constructed with a maximum time difference ΔT between *in situ* measurements and satellite overpass. Consistently with previous analysis [Zibordi *et al.* 2018], satellite reduced-resolution (RR) data were retained for matchup construction when all the 3×3 image elements centered at the *in situ* measurement locations satisfied the following criteria: *i*. data were not affected by cloud contamination and in general by any of the main exclusion flags; *ii*. the satellite viewing angle θ was lower than 65° and the sun zenith angle θ_0 lower than 70°; *iii*. the coefficients of variation of both L_{WN} at 560 nm and aerosol optical depth τ_a at 865 nm, were lower than 0.2.

The comparison results are summarized through *i.* the median of relative (signed) percent differences ψ_m between remote sensing and *in situ* data (as an index for biases), and *ii.* the median of absolute (unsigned) percent differences $|\psi|_m$ (as an index for dispersion). Additional statistical quantities provided to better support the data analysis are the root mean square of differences *rmsd* (with the same units of the quantity considered), the coefficient of determination r^2, the median of differences Δ_m and the median of absolute differences $|\Delta|_m$.

The former statistical indices are expected to provide accurate results with a significant number of match-ups that would minimize the effects of *i.* differences between *in situ* and satellite spatial resolutions, *ii.* sub-pixel spatial variability in satellite observations and *iii.* temporal changes in seawater and atmospheric optical properties occurring between satellite and *in situ* data collection.

The OLCI L_{WN} data, L_{WN}^{OLCI}, assessed in this study were computed from the spectral reflectance ρ^{OLCI} included in the standard Level-2 products, according to

$$L_{WN}^{OLCI} = \rho^{OLCI} \frac{E_0}{\pi} C_{f/Q}$$

where E_0 is the mean extraterrestrial solar irradiance [Thuillier et al. 2003] and $C_{f/Q}$ accounts for the bidirectional effects [EUMETSAT 2108, Zibordi et al. 2009b].

In agreement with previous investigations [Zibordi *et al.* 2018], additional OLCI products assessed in the study are τ_a at 865 nm and the Ångström exponent α.

It is expected that the *in situ* AERONET-OC data applied in this analysis well represent the atmospheric and marine optical properties of most of the European marine regions.

In summary the inter-comparison focusses on L_{WN}, τ_a and α over 7 sites: the Acqua Alta Oceanographic Tower (AAOT) in the northern Adriatic Sea representative of moderately sediment dominated waters; Galata (GLT) and Gloria (GLR) in the Western Black Sea embracing waters dominated by variable concentrations of sediments and colored dissolved organic matter (CDOM); Gustaf Dalen (GDLT), Helsinki (HLT) and Irbe (ILT) Lighthouses in the Baltic Proper and in the Gulf of Finland representative of highly CDOM dominated waters, and finally Casablanca (CPL) in the Western Mediterranean Sea representative of open sea chlorophyll dominated waters. The aerosol type is mostly continental with maritime influence at all the sites [Mélin et al. 2013].

It is mentioned that the *in situ* L_{WN} applied in the analysis are restricted to the measurements closest in time to the satellite overpass, and are band-shifted [Zibordi et al. 2009b] to match the OLCI center-wavelengths and consequently minimize the impact of differences between corresponding, but not exactly matching, spectral bands.

The values of α for OLCI are determined from NIR bands centered at 779 and 865 nm. The *in situ* AERONET-OC values of α were determined from τ_a at 665, 779 and 870 nm.

4 Results and Discussion

The matchups of *in situ* and satellite data were constructed applying a maximum time difference ΔT of ±2hr for AERONET-OC data. Still, generally more than 80% of the time differences are within ±1hr.

The so-called ANNOT flags provided with OLCI data products [EUMETSAT 2018] and recommended for validation exercises, were not accounted for in the construction of matchups. In fact, while they do not have any significant impact on the analysis of data from open sea regions, they may lead to the exclusion of a large number of *in situ* – satellite matchups (i.e., from 60 to 90% when applying ANNOT_DROUT) from optically complex regions mostly associated with relatively high values of L_{WN}.

Comparison results are presented in Fig.s 7-34. These include figures for each JRC AERONET-OC site, labelled as *Overview* and *Details*. The former aim at providing a general view of the comparison results for the various quantities. The latter aim at detailing results on radiometric data products through scatter plots of satellite derived (i.e., OLCI) and in situ (i.e., AERONET-OC indicated as PRS) values of the normalized-water leaving radiance L_{WN}.

4.1 Normalized Water-Leaving Radiance

The qualitative comparison of *in situ* and satellite L_{WN} spectra is shown in panels (a) and (b) of the *Overview* figures. The main purpose of such a comparison is to illustrate the type of spectra included in the analysis and to show artifacts that may characterize either satellite or *in situ* data.

The spectra indicate a fair qualitative agreement between *in situ* and satellite data. Still, striking is the presence of negative L_{WN} affecting both OLCI-A and OLCI-B data in the blue spectral bands at the GDLT, ILT and HLT sites characterized by very low values of water-leaving radiance due to CDOM absorption.

Quantitative comparisons between satellite and *in situ* data are presented in panels (a)–(f) of the *Details* figures through individual scatter plots for each spectral band. Notably, the AAOT data do not show any significant impact of negative radiances at the blue bands. However, a high occurrence of OLCI-A (but not OLCI-B) negative L_{WN} data is observed for GLT and GLR in the Black Sea. Specifically, negative L_{WN} appear at several spectral bands in the blue and red. An analysis restricted to the spectra exhibiting those negative radiances, shows that they mostly pertain to CDOM dominated waters (i.e., exhibiting L_{WN} spectra with maxima at 560 nm, and relative minima at 400 nm and 665 nm). This finding is fully supported by the scatter plots proposed for GDLT, ILT and HLT. Still, regardless of the water type, it is expected that the negative L_{WN} often observed in the Baltic and Black Seas, are the result of an overcorrection of the atmospheric effects. This interpretation is supported by the similarity observed among the scatter plots of τ_a and α proposed for the different marine regions (see sub-section 4.2).

An evaluation of biases through ψ_m indicates values largely varying with the amplitude of L_{WN}, with minima generally within a few percent at 560 nm for both OLCI-A and OLCI-B.

In summary, OLCI-A data products indicate a general underestimate of L_{WN} while OLCI-B products exhibit an overestimate. This is clearly evident for chlorophyll-a dominated waters from results presented for the CPL site in Fig.s 19-22.

Overall results from the analysis of the OLCI-A L_{WN} indicate large (qualitative) equivalence with findings from the assessment of MERIS Level-2 data from the 3rd reprocessing [Zibordi *et al* 2013]. Similarly, OLCI-B L_{WN} indicates large (qualitative) equivalence with findings from the assessment of MERIS Level-2 data from the 2nd reprocessing.

4.2 Aerosol optical thickness

The aerosol products τ_a and α, which are by-products of the atmospheric correction, may likely provide insight on the correction process or on the calibration accuracy of the NIR bands applied to determine the aerosol type. Comparisons between satellite and *in situ* atmospheric products are illustrated in panels (e) and (f) of the *Overview* figures.

Results show a systematic overestimate of τ_a at 865 nm that generally exceeds 50% for both OLCI-A and OLCI-B. Notably, the values of α from both OLCI-A and OLCI-B do not exhibit any correlation with the *in situ* values, and show a very narrow distribution below a maximum of approximately 1.7. This indicates issues in the accurate determination of the aerosol type likely heavily impacting the atmospheric correction process.

4.3 On the application of ANNOT Flags

The application of a number of annotation flags, i.e., ANNOT, have been recommended for validation purposes (EUMETSAT 2019). Mostly, the ANNOT Flags are proposed as quality indices. Thus they support a quality control process. This means that the ANNOT Flags are largely expected to support data users on the quality screening of the final data products.

However, validation is a quality assurance process. It should specifically evaluate the quality of the data products in view of improving them. This implies the need to assess the quality of data through fully independent means (e.g., independent data, which would be contradicted by the application of information resulting from the atmospheric correction itself). Because of this, the ANNOT Flags should not be applied in the validation of data products, which is a quality assurance process.

An evaluation of the impact of ANNOT Flags is presented in Fig.s 35 and 36.

Table 2. Annotation flags (ANNOT Flags) providing indication on the performance of the atmospheric correction process. The flags highlighted in blue are those recommended to exclude poor-quality data during validation processes. DROUT is the flag exhibiting the largest impact, especially in optically complex regions.

ANGSTROM (Ångström exponent cannot be computed);
AERO_B (blue aerosols);
ABSO_D (desert dust absorbing aerosols);
ACLIM (aerosol model does not match aerosol climatology);
ABSOA (absorbing aerosols);
MIXR1 (aerosol mixing ratio is equal to 0 or 1);
DROUT (minimum absolute value of the reflectance error at 510 nm is greater than a defined threshold);
TAU06 (aerosol optical thickness is greater than a defined threshold).

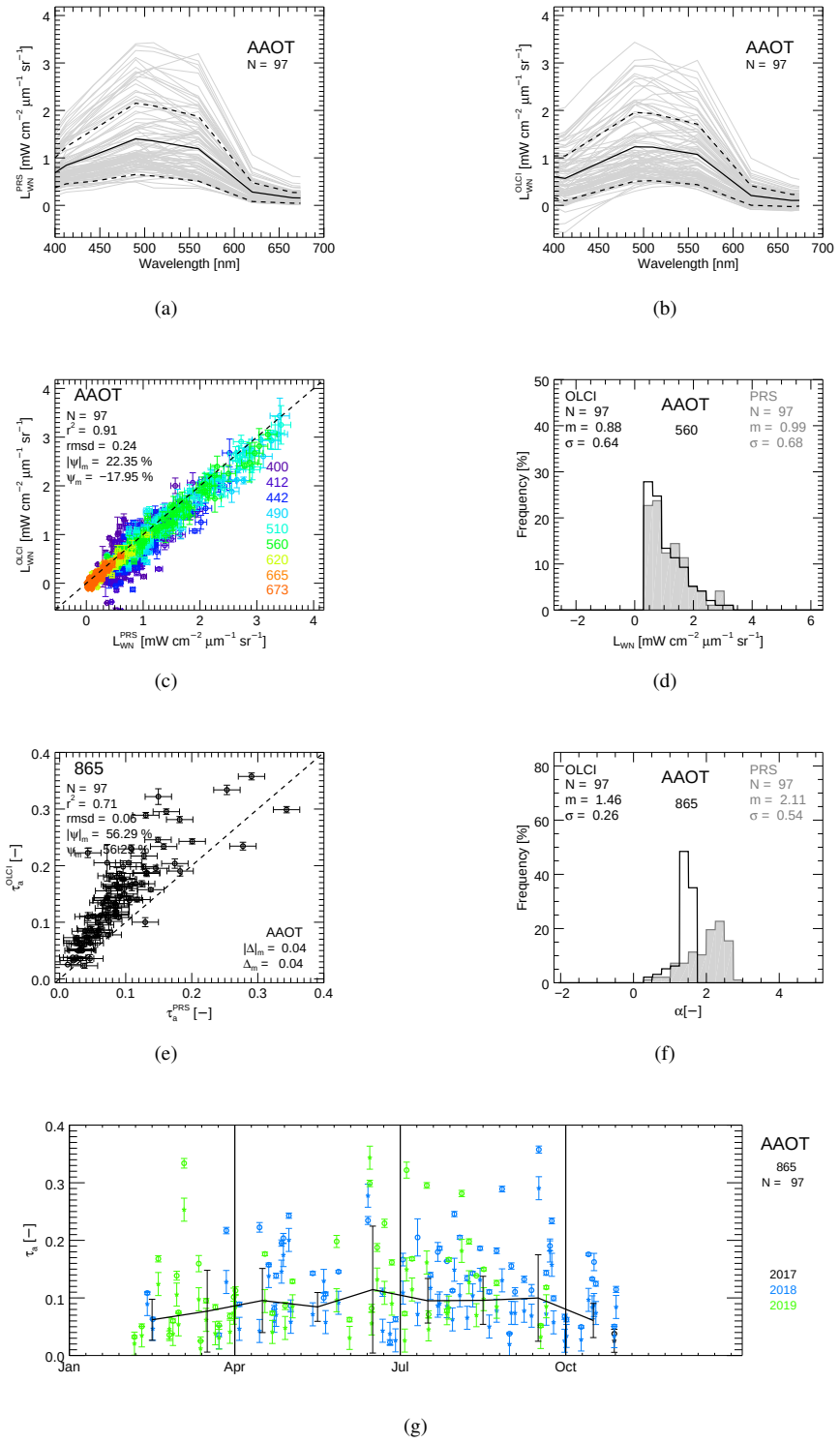

Figure 7: **[S3A@AAOT Overview]** OLCI-A assessment at the AAOT site: (a) PRS L_{WN} spectra, (b) OLCI-A L_{WN} spectra, (c) OLCI-A versus PRS L_{WN} scatter plot, (d) frequency distribution of OLCI-A and PRS L_{WN} at 560 nm, (e) OLCI-A versus PRS τ_a at 865 nm, (f) frequency distribution of OLCI-A and PRS α, (g) yearly distribution of OLCI-A τ_a at 865 nm. The continuous and dashed lines in panels (a) and (b) indicate the mean and ± 1 standard deviation, respectively. The error bars associated to *in situ* data indicate measurement uncertainties while those related to satellite data products indicate the variation coefficient determined from the 3×3 elements applied for matchups construction.

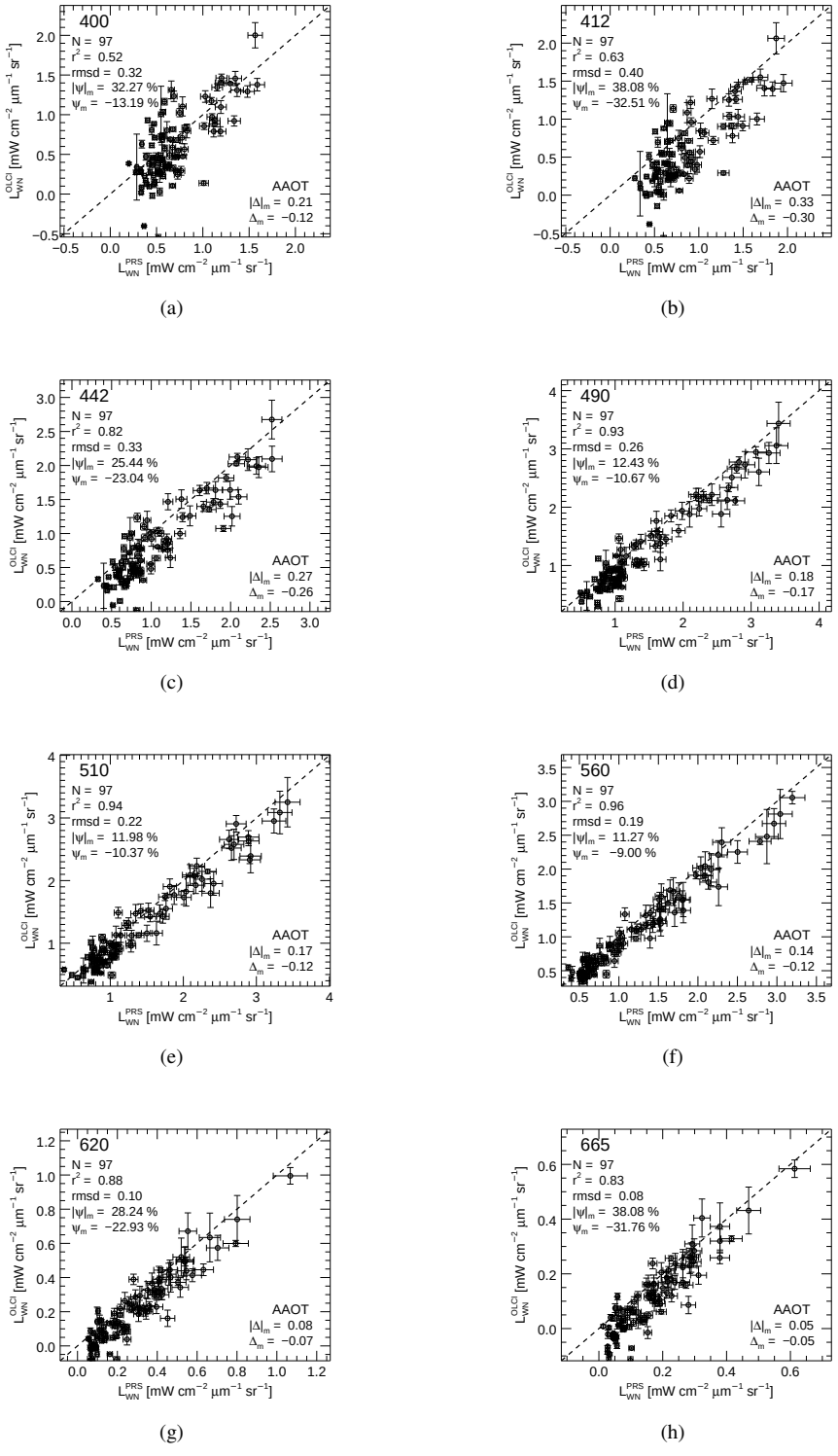

Figure 8: **[S3A@AAOT Details]** OLCI-A assessment at the AAOT site. Panels display scatter plot of OLCI-A versus PRS L_{WN} at different center-wavelengths: (a) 400, (b) 412, (c) 442, (d) 490, (e) 510, (f) 560, (g) 620, (h) 665 nm. The error bars associated to *in situ* data indicate measurement uncertainties while those related to satellite data products indicate the variation coefficient determined from the 3×3 elements applied for matchups construction.

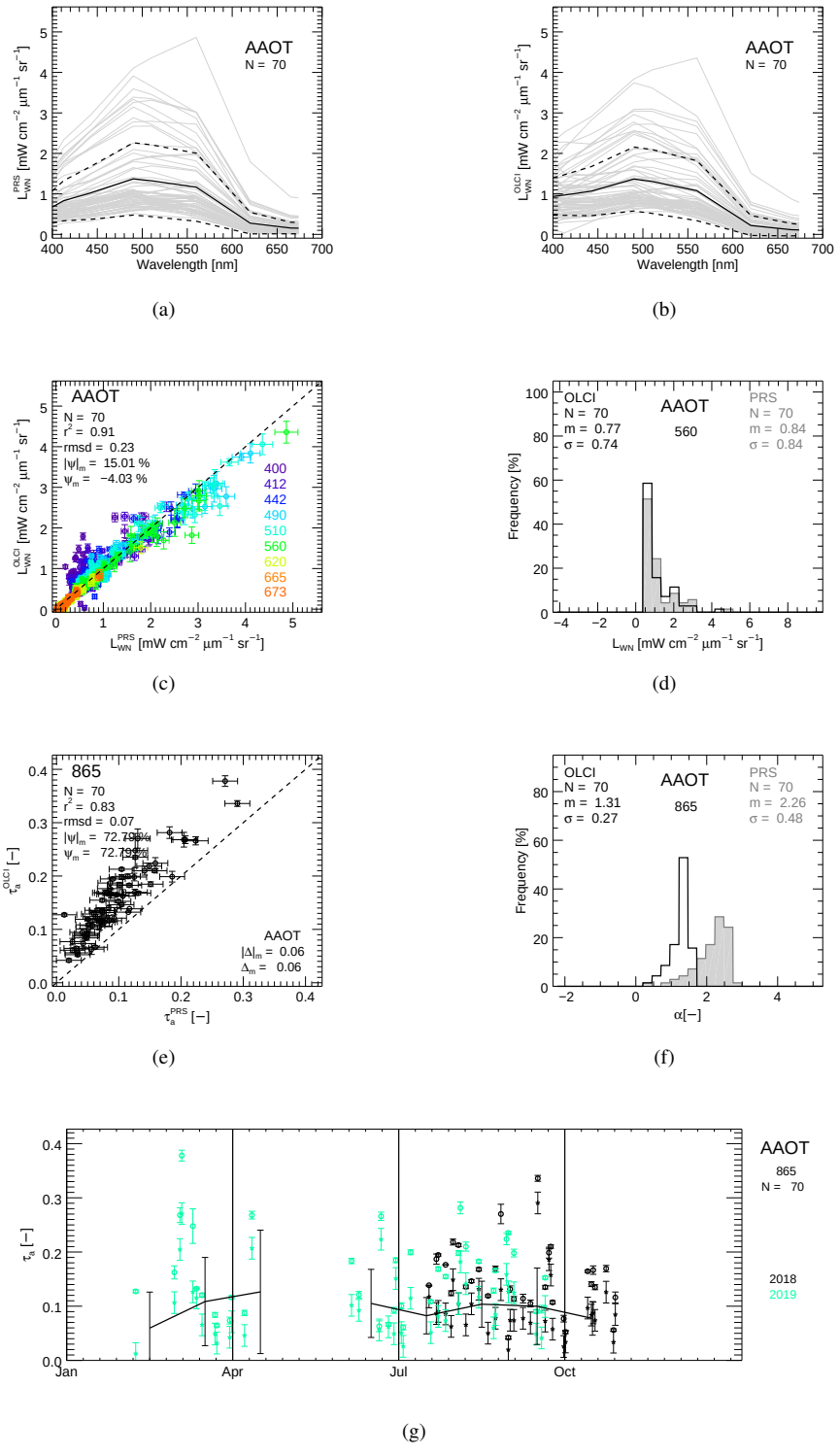

Figure 9: **[S3B@AAOT Overview]** OLCI-B assessment at the AAOT site: (a) PRS L_{WN} spectra, (b) OLCI-B L_{WN} spectra, (c) OLCI-B versus PRS L_{WN} scatter plot, (d) frequency distribution of OLCI-B and PRS L_{WN} at 560 nm, (e) OLCI-B versus PRS τ_a at 865 nm, (f) frequency distribution of OLCI-B and PRS α, (g) yearly distribution of OLCI-B τ_a at 865 nm. The continuous and dashed lines in panels (a) and (b) indicate the mean and ± 1 standard deviation, respectively. The error bars associated to *in situ* data indicate measurement uncertainties while those related to satellite data products indicate the variation coefficient determined from the 3×3 elements applied for matchups construction.

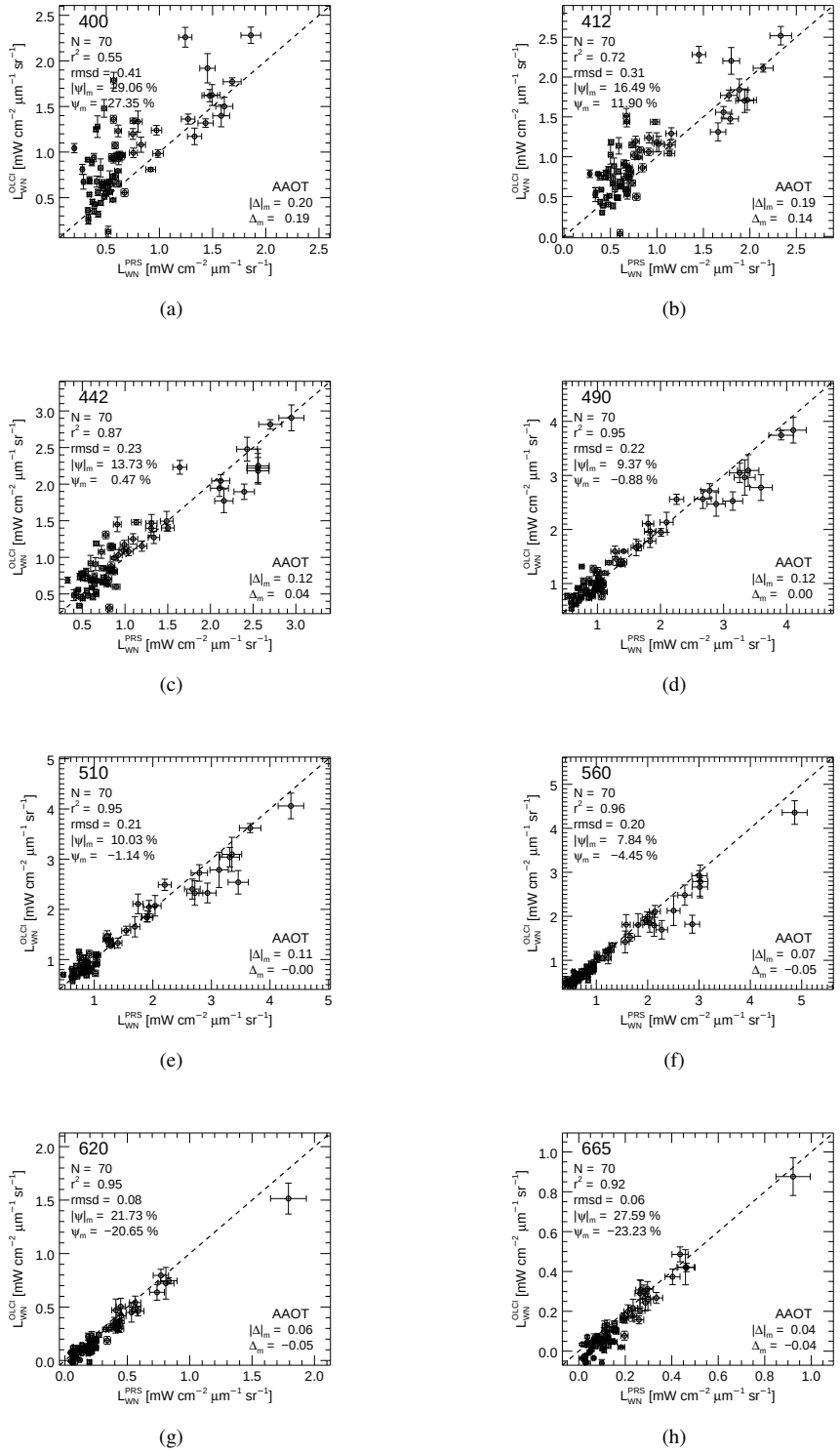

Figure 10: **[S3B@AAOT Details]** OLCI-B assessment at the AAOT site. Panels display scatter plot of OLCI-B versus PRS L_{WN} at different center-wavelengths: (a) 400, (b) 412, (c) 442, (d) 490, (e) 510, (f) 560, (g) 620, (h) 665 nm. The error bars associated to *in situ* data indicate measurement uncertainties while those related to satellite data products indicate the variation coefficient determined from the 3×3 elements applied for matchups construction.

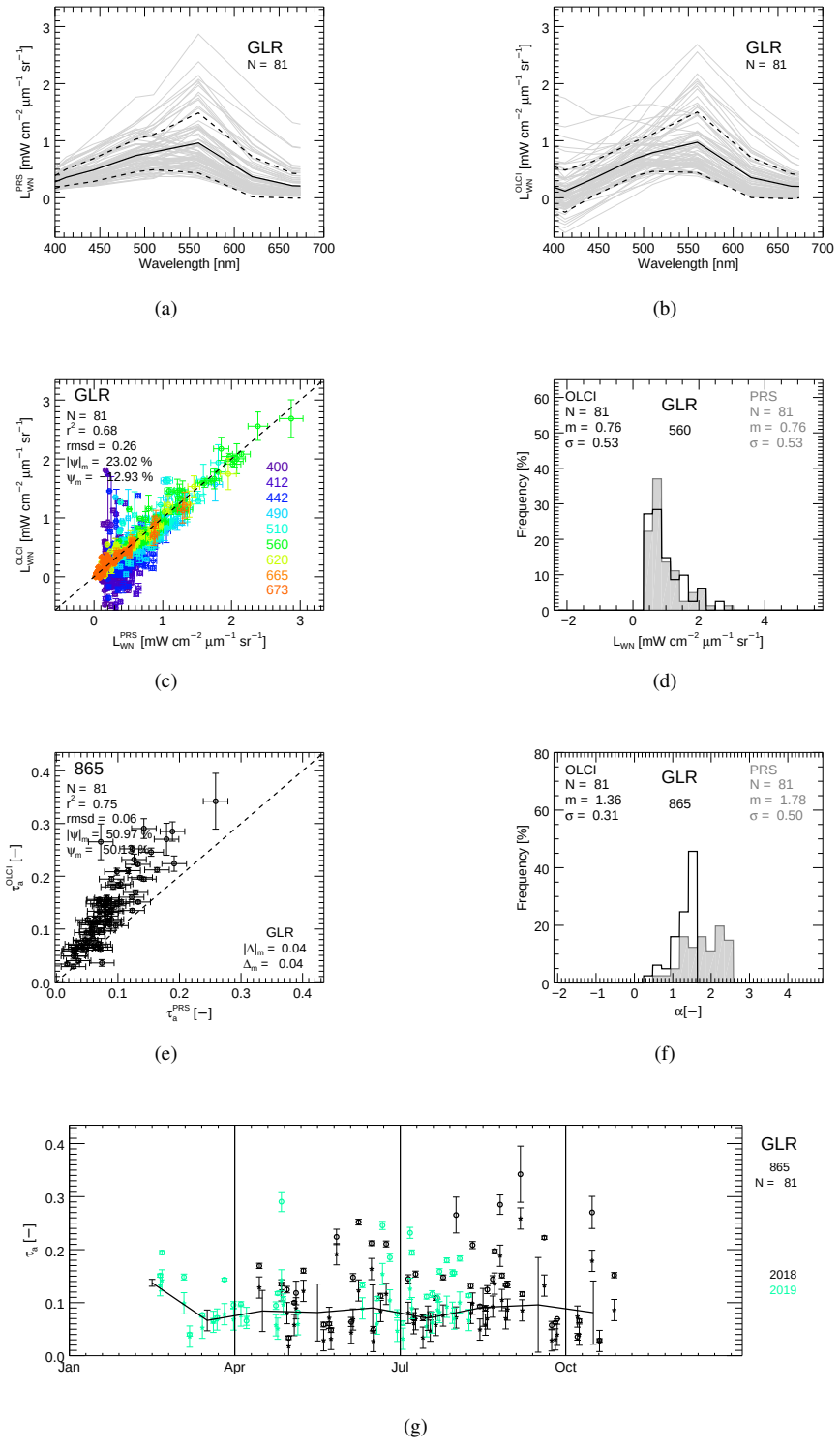

Figure 11: **[S3A@GLR Overview]** OLCI-A assessment at the GLR site: (a) PRS L_{WN} spectra, (b) OLCI-A L_{WN} spectra, (c) OLCI-A versus PRS L_{WN} scatter plot, (d) frequency distribution of OLCI-A and PRS L_{WN} at 560 nm, (e) OLCI-A versus PRS τ_a at 865 nm, (f) frequency distribution of OLCI-A and PRS α, (g) yearly distribution of OLCI-A τ_a at 865 nm. The continuous and dashed lines in panels (a) and (b) indicate the mean and ± 1 standard deviation, respectively. The error bars associated to *in situ* data indicate measurement uncertainties while those related to satellite data products indicate the variation coefficient determined from the 3×3 elements applied for matchups construction.

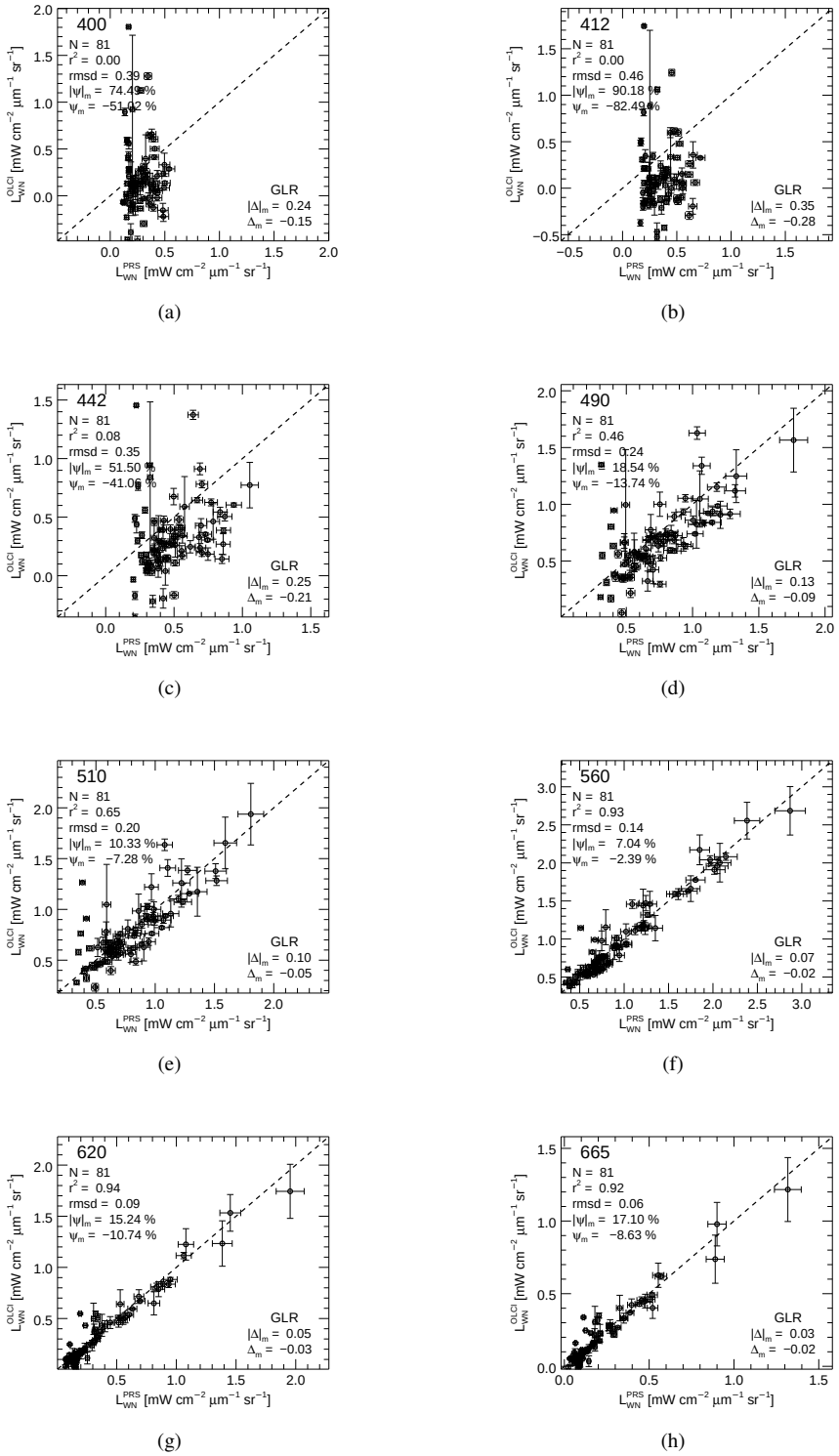

Figure 12: **[S3A@GLR Details]** OLCI-A assessment at the GLR site. Panels display scatter plot of OLCI-A versus PRS L_{WN} at different center-wavelengths: (a) 400, (b) 412, (c) 442, (d) 490, (e) 510, (f) 560, (g) 620, (h) 665 nm. The error bars associated to *in situ* data indicate measurement uncertainties while those related to satellite data products indicate the variation coefficient determined from the 3×3 elements applied for matchups construction.

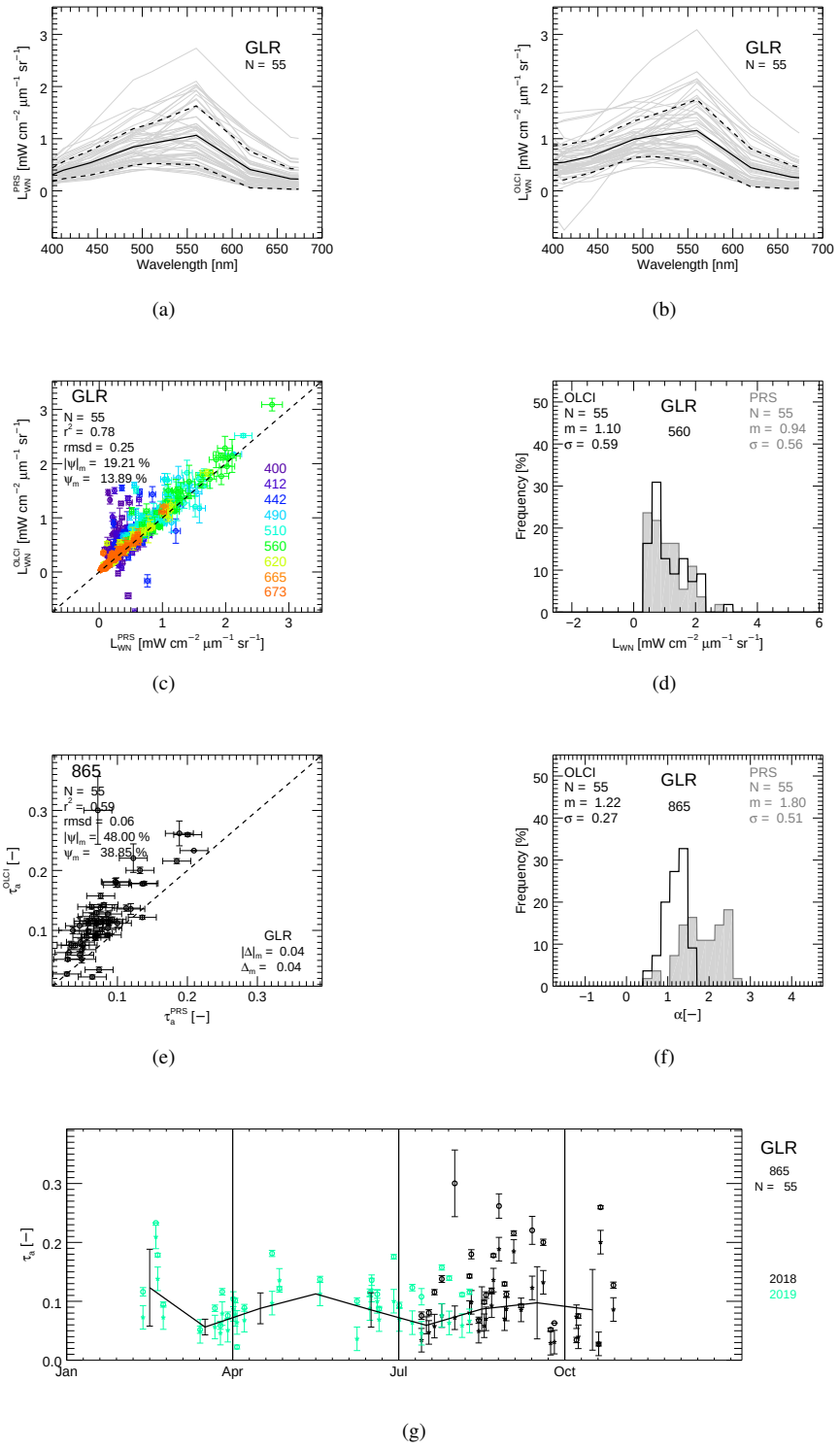

Figure 13: **[S3B@GLR Overview]** OLCI-B assessment at the GLR site: (a) PRS L_{WN} spectra, (b) OLCI-B L_{WN} spectra, (c) OLCI-B versus PRS L_{WN} scatter plot, (d) frequency distribution of OLCI-B and PRS L_{WN} at 560 nm, (e) OLCI-B versus PRS τ_a at 865 nm, (f) frequency distribution of OLCI-B and PRS α, (g) yearly distribution of OLCI-B τ_a at 865 nm. The continuous and dashed lines in panels (a) and (b) indicate the mean and ± 1 standard deviation, respectively. The error bars associated to *in situ* data indicate measurement uncertainties while those related to satellite data products indicate the variation coefficient determined from the 3×3 elements applied for matchups construction.

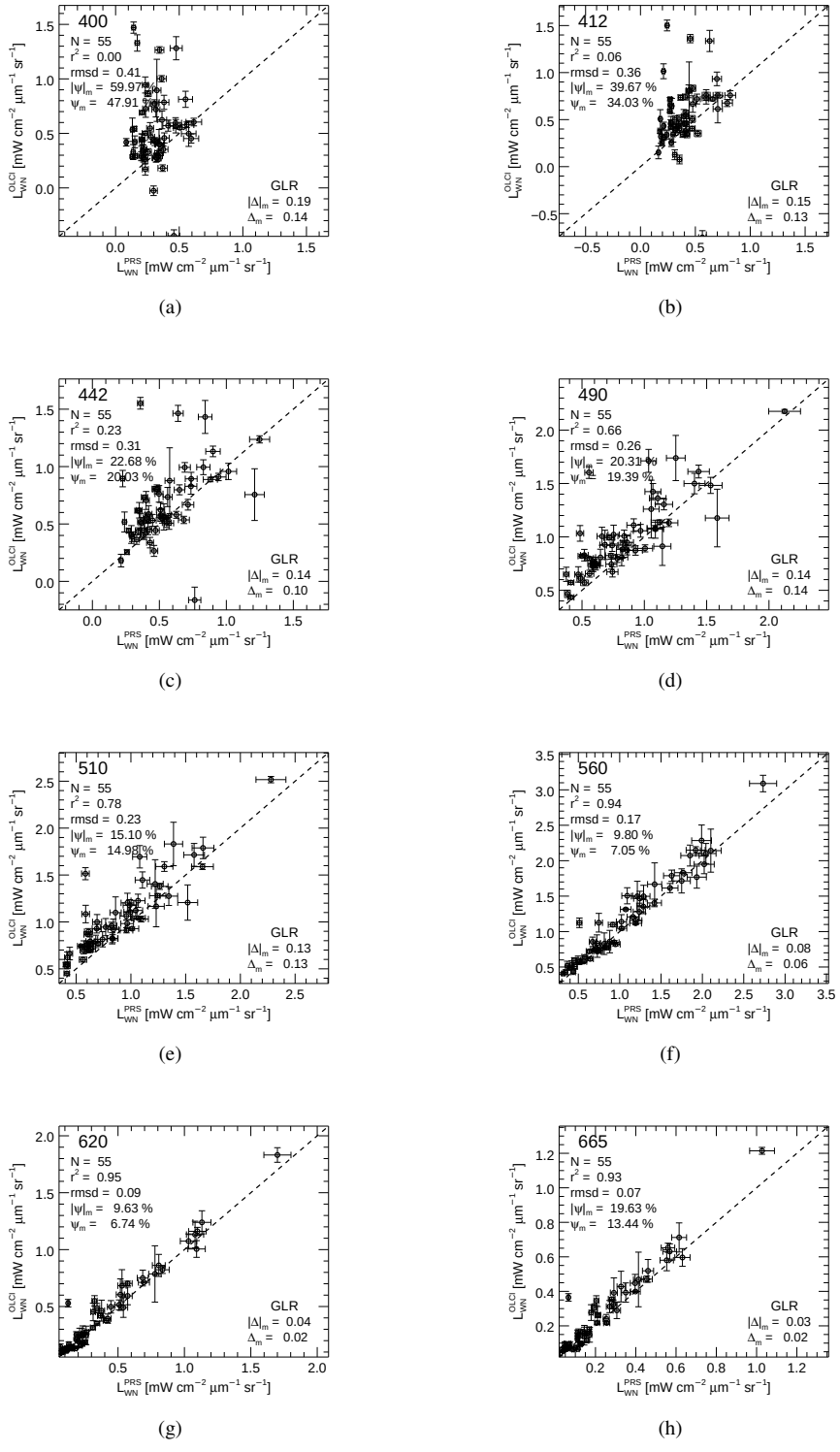

Figure 14: **[S3B@GLR Details]** OLCI-B assessment at the GLR site. Panels display scatter plot of OLCI-B versus PRS L_{WN} at different center-wavelengths: (a) 400, (b) 412, (c) 442, (d) 490, (e) 510, (f) 560, (g) 620, (h) 665 nm. The error bars associated to *in situ* data indicate measurement uncertainties while those related to satellite data products indicate the variation coefficient determined from the 3×3 elements applied for matchups construction.

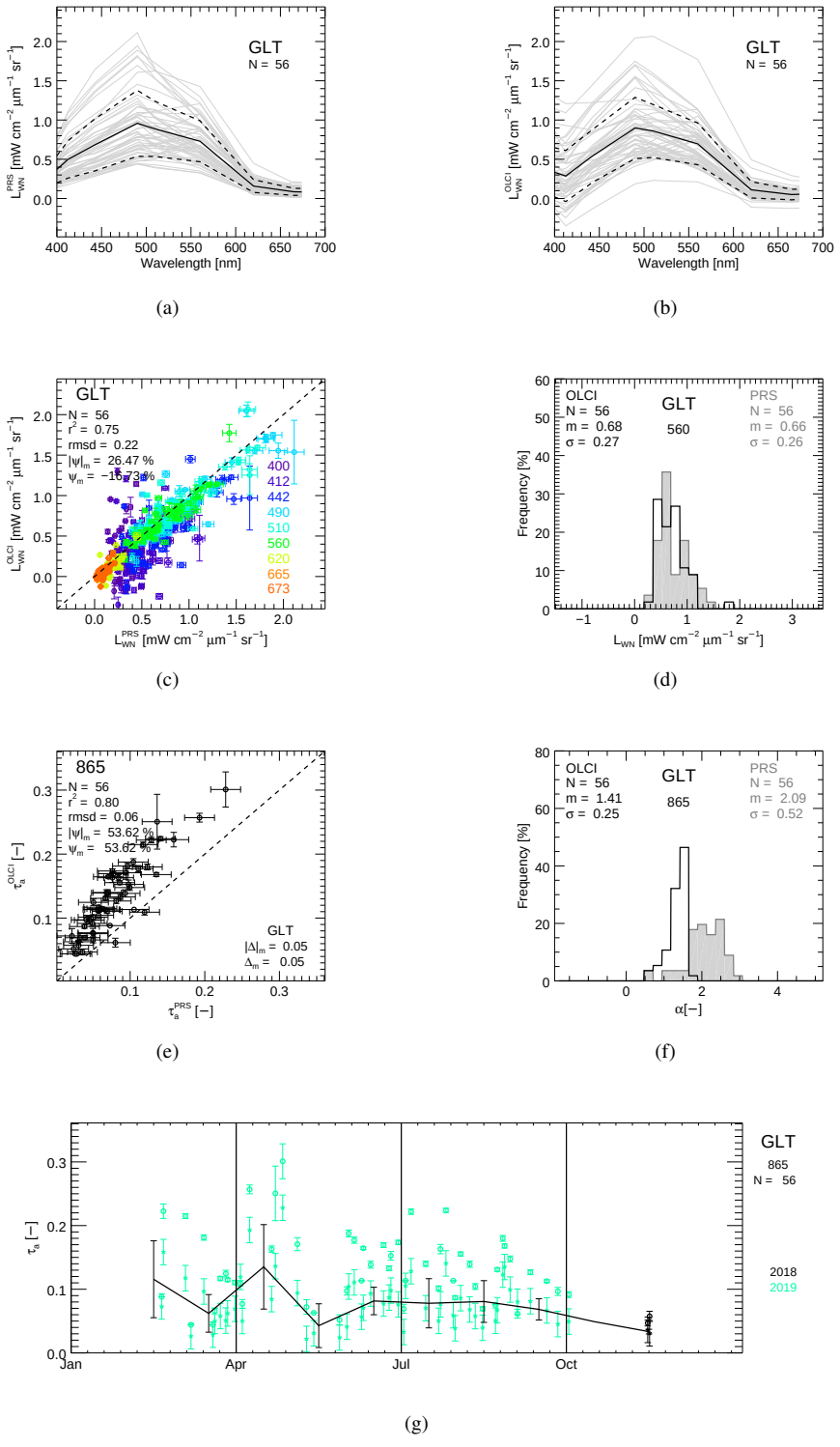

Figure 15: **[S3A@GLT Overview]** OLCI-A assessment at the GLT site: (a) PRS L_{WN} spectra, (b) OLCI-A L_{WN} spectra, (c) OLCI-A versus PRS L_{WN} scatter plot, (d) frequency distribution of OLCI-A and PRS L_{WN} at 560 nm, (e) OLCI-A versus PRS τ_a at 865 nm, (f) frequency distribution of OLCI-A and PRS α, (g) yearly distribution of OLCI-A τ_a at 865 nm. The continuous and dashed lines in panels (a) and (b) indicate the mean and ± 1 standard deviation, respectively. The error bars associated to *in situ* data indicate measurement uncertainties while those related to satellite data products indicate the variation coefficient determined from the 3×3 elements applied for matchups construction.

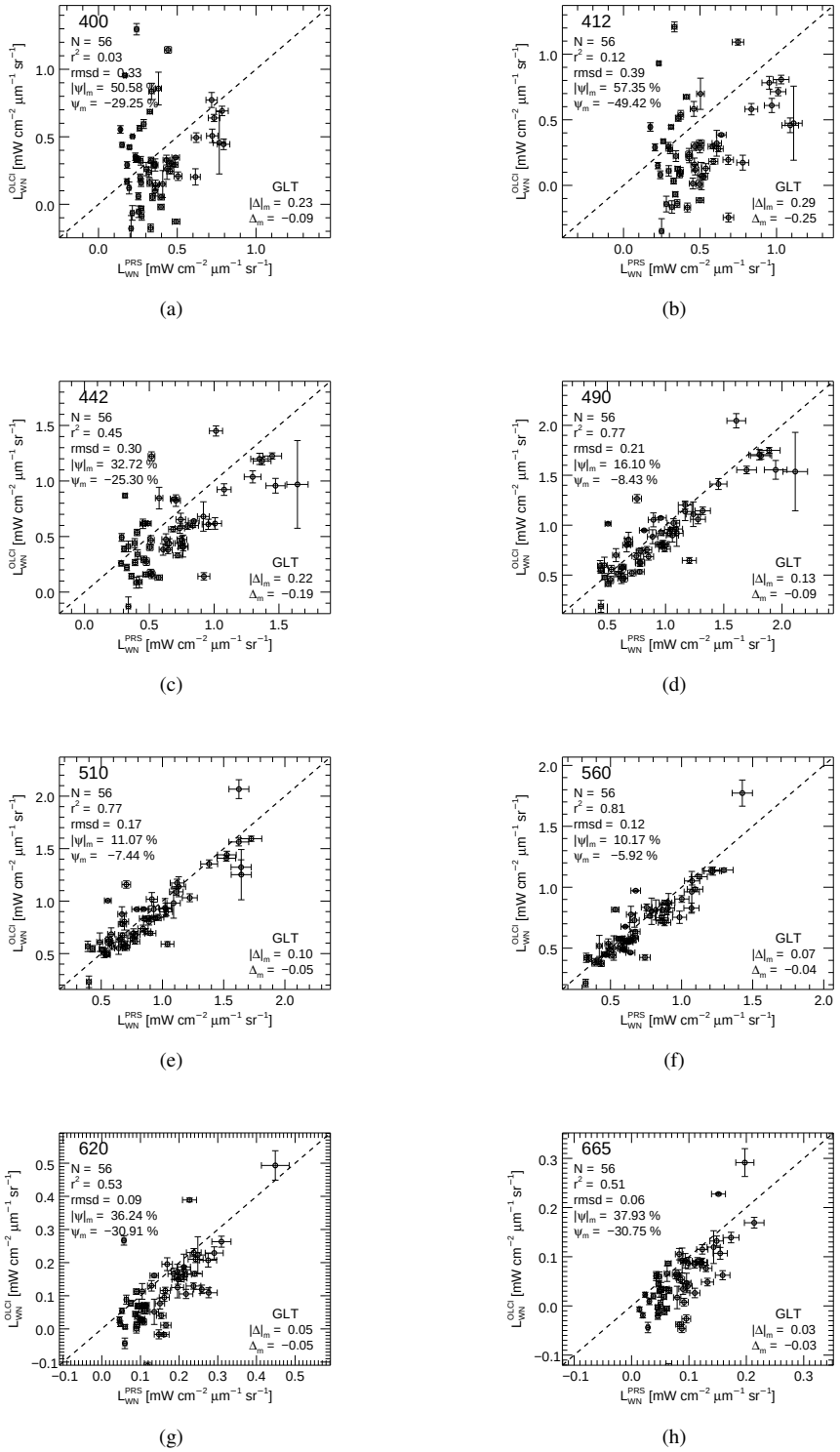

Figure 16: **[S3A@GLT Details]** OLCI-A assessment at the GLT site. Panels display scatter plot of OLCI-A versus PRS L_{WN} aat different center-wavelengths: (a) 400, (b) 412, (c) 442, (d) 490, (e) 510, (f) 560, (g) 620, (h) 665 nm. The error bars associated to *in situ* data indicate measurement uncertainties while those related to satellite data products indicate the variation coefficient determined from the 3×3 elements applied for matchups construction.

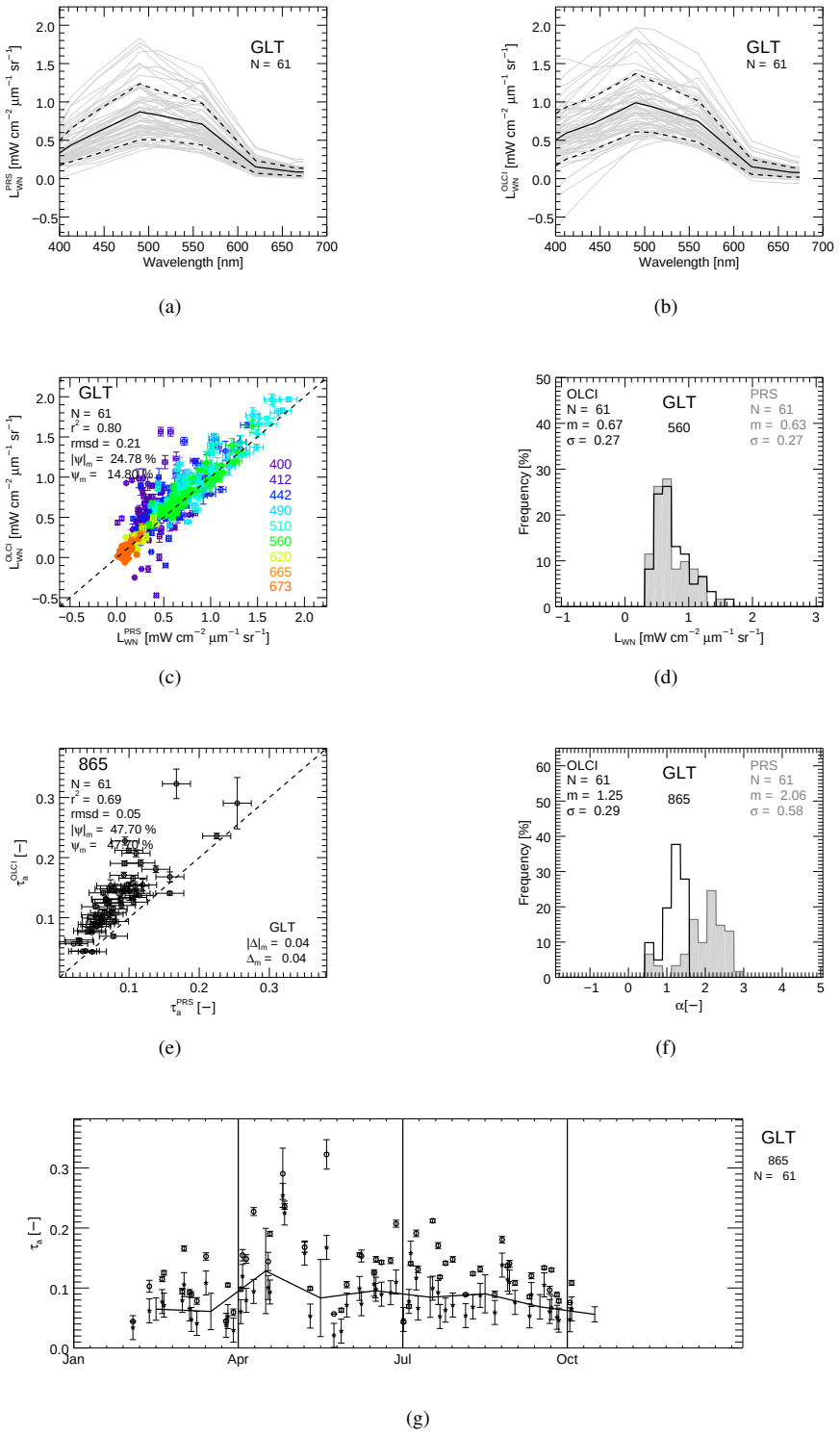

Figure 17: **[S3B@GLT Overview]** OLCI-B assessment at the GLT site: (a) PRS L_{WN} spectra, (b) OLCI-B L_{WN} spectra, (c) OLCI-B versus PRS L_{WN} scatter plot, (d) frequency distribution of OLCI-B and PRS L_{WN} at 560 nm, (e) OLCI-B versus PRS τ_a at 865 nm, (f) frequency distribution of OLCI-B and PRS α, (g) yearly distribution of OLCI-B τ_a at 865 nm. The continuous and dashed lines in panels (a) and (b) indicate the mean and ± 1 standard deviation, respectively. The error bars associated to *in situ* data indicate measurement uncertainties while those related to satellite data products indicate the variation coefficient determined from the 3×3 elements applied for matchups construction.

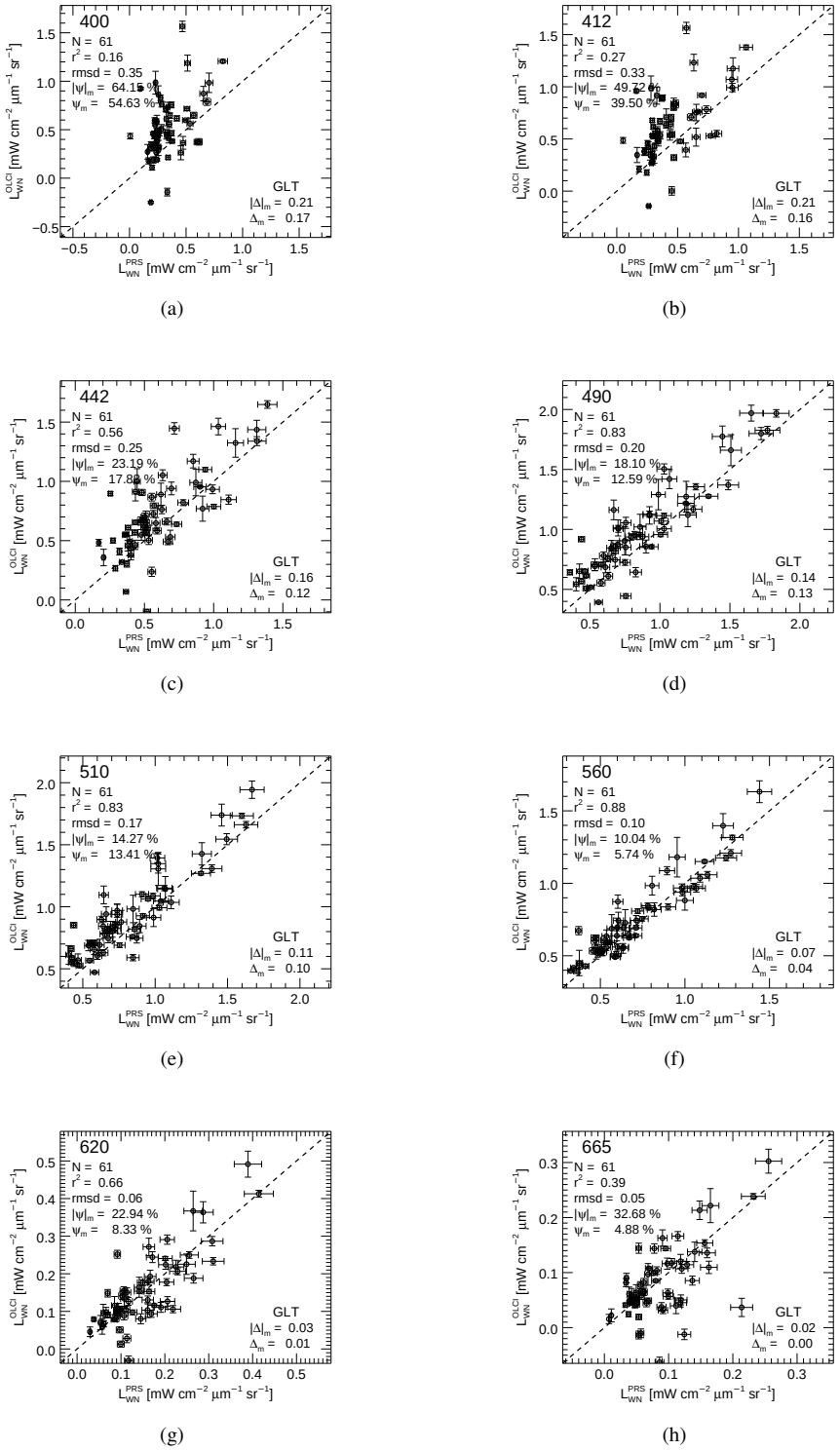

Figure 18: **[S3B@GLT Details]** OLCI-B assessment at the GLT site. Panels display scatter plot of OLCI-B versus PRS L_{WN} at different center-wavelengths: (a) 400, (b) 412, (c) 442, (d) 490, (e) 510, (f) 560, (g) 620, (h) 665 nm. The error bars associated to *in situ* data indicate measurement uncertainties while those related to satellite data products indicate the variation coefficient determined from the 3×3 elements applied for matchups construction.

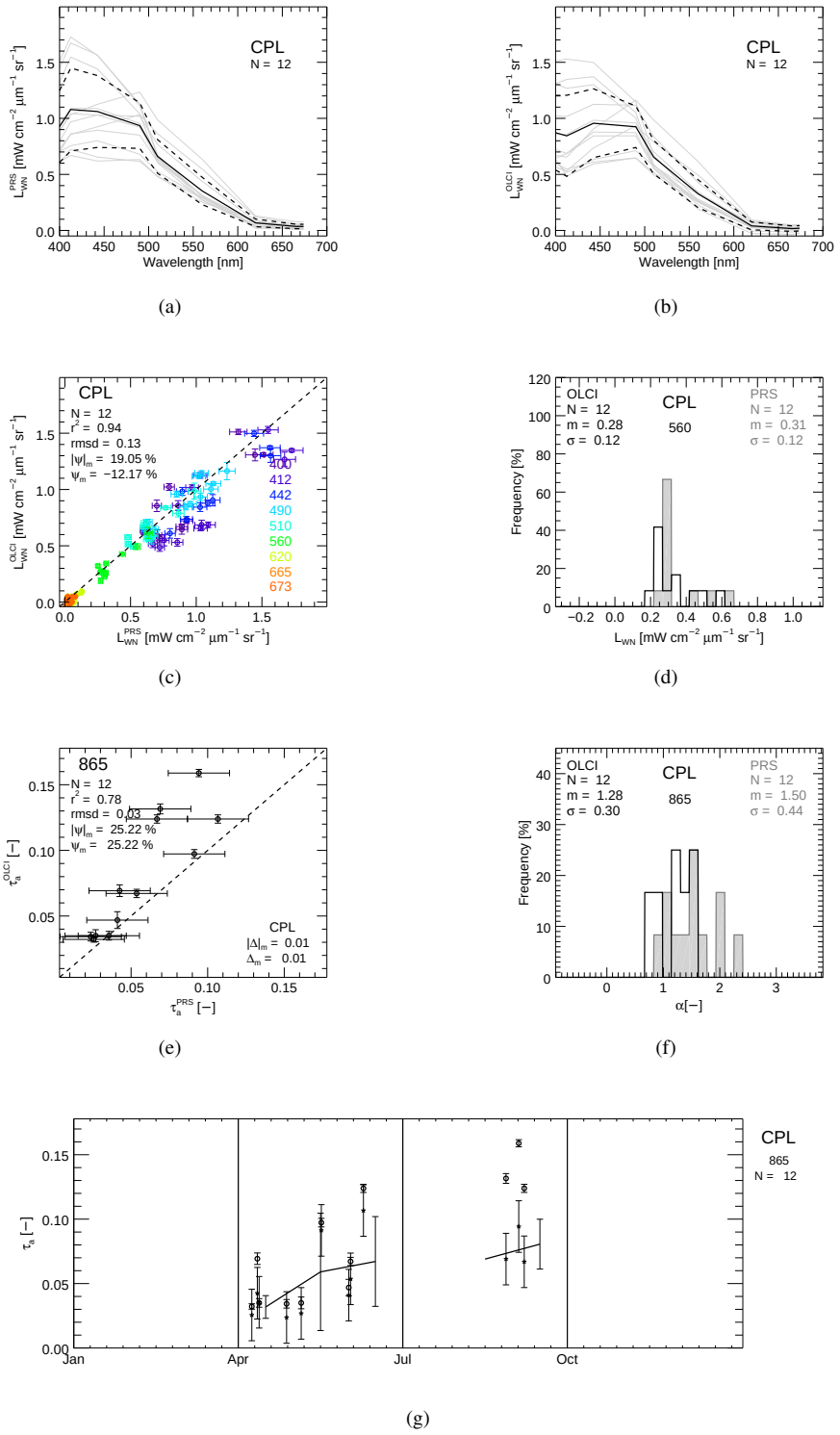

Figure 19: **[S3A@CPL Overview]** OLCI-A assessment at the GLT site: (a) PRS L_{WN} spectra, (b) OLCI-A L_{WN} spectra, (c) OLCI-A versus PRS L_{WN} scatter plot, (d) frequency distribution of OLCI-A and PRS L_{WN} at 560 nm, (e) OLCI-A versus PRS τ_a at 865 nm, (f) frequency distribution of OLCI-A and PRS α, (g) yearly distribution of OLCI-A τ_a at 865 nm. The continuous and dashed lines in panels (a) and (b) indicate the mean and ± 1 standard deviation, respectively. The error bars associated to *in situ* data indicate measurement uncertainties while those related to satellite data products indicate the variation coefficient determined from the 3×3 elements applied for matchups construction.

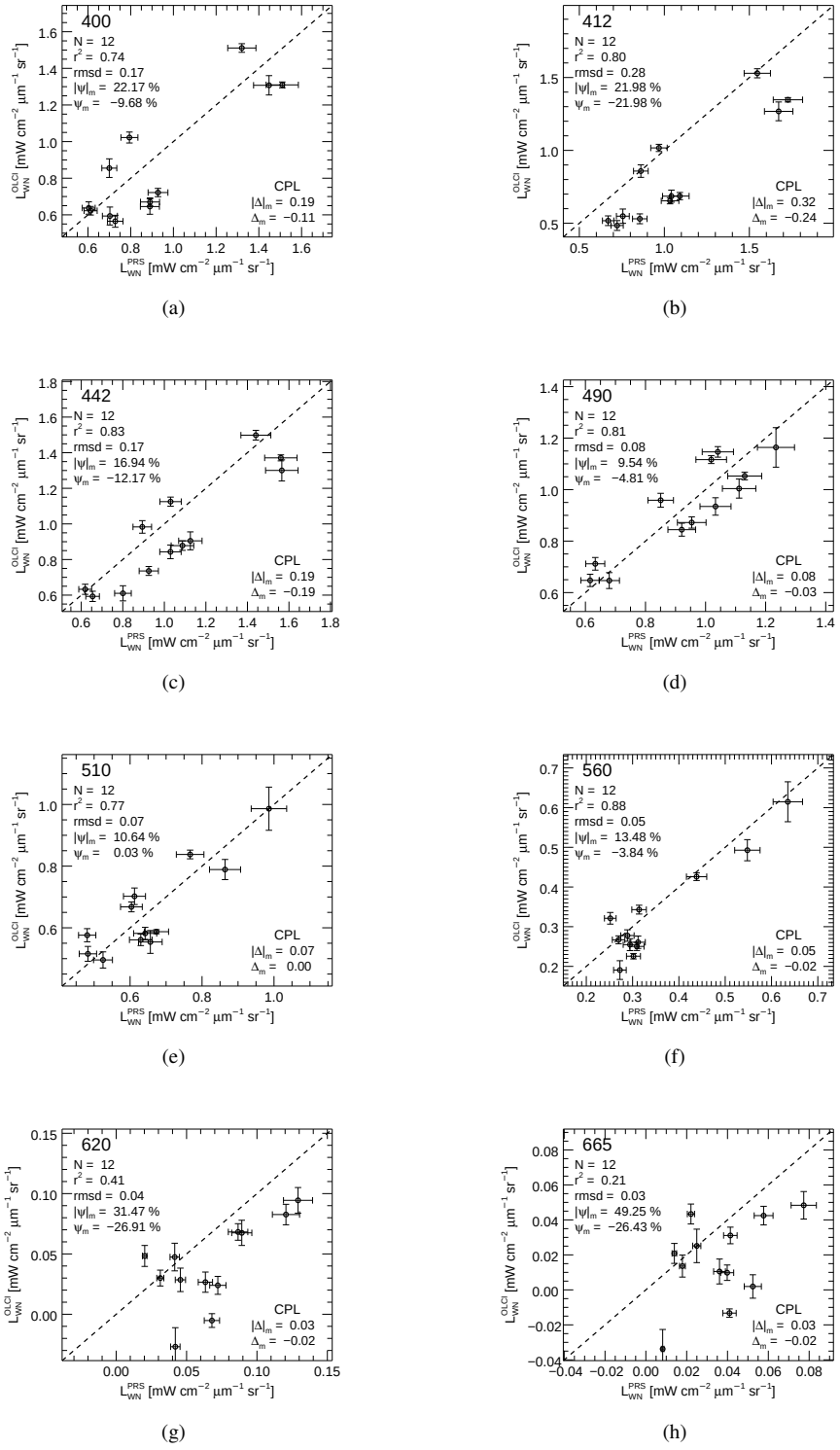

Figure 20: **[S3A@CPL Details]** OLCI-A assessment at the CPL site. Panels display scatter plot of OLCI-A versus PRS L_{WN} at different center-wavelengths: (a) 400, (b) 412, (c) 442, (d) 490, (e) 510, (f) 560, (g) 620, (h) 665 nm. The error bars associated to *in situ* data indicate measurement uncertainties while those related to satellite data products indicate the variation coefficient determined from the 3×3 elements applied for matchups construction.

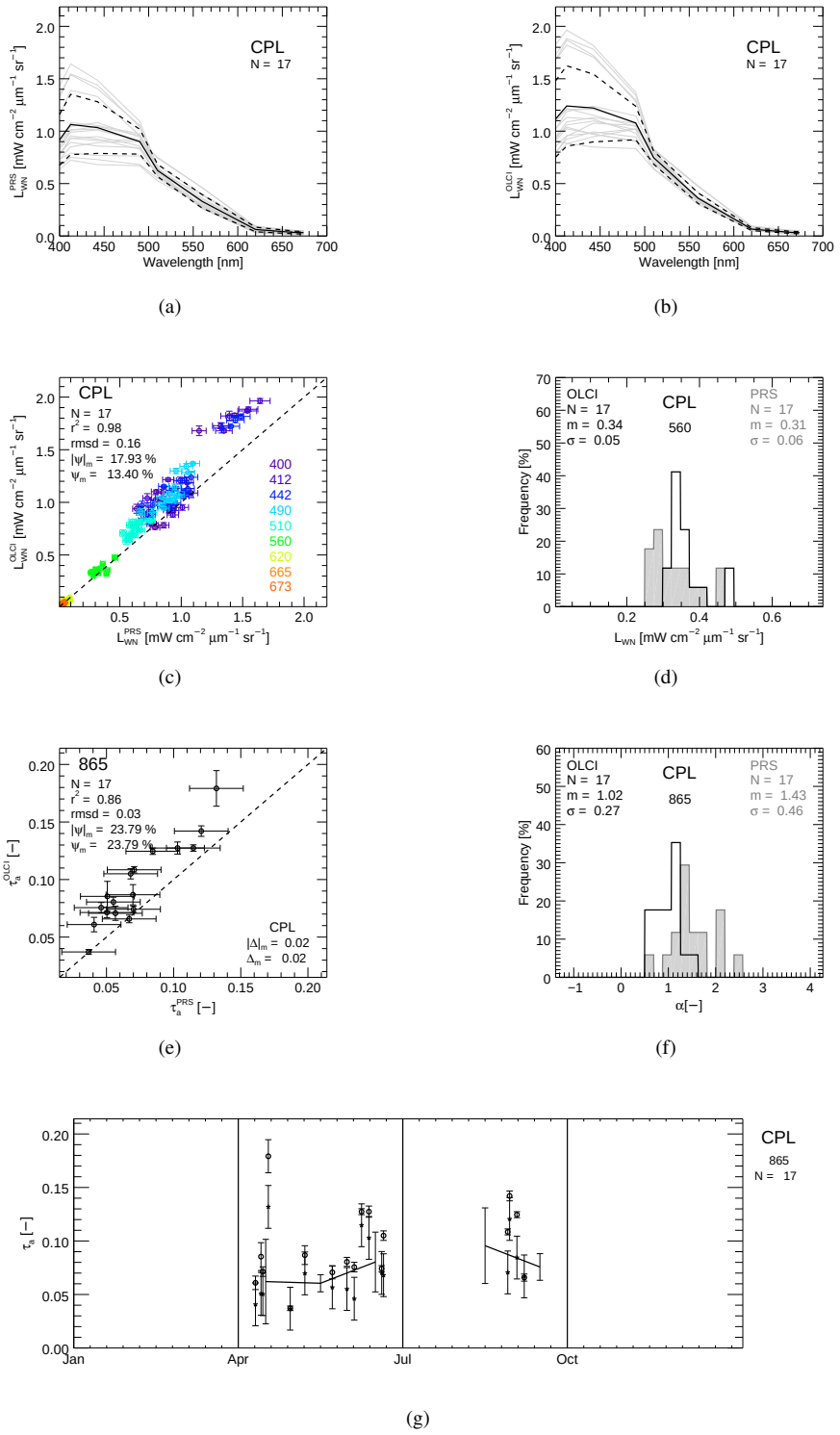

Figure 21: **[S3B@CPL Overview]** OLCI-B assessment at the CPL site: (a) PRS L_{WN} spectra, (b) OLCI-B L_{WN} spectra, (c) OLCI-B versus PRS L_{WN} scatter plot, (d) frequency distribution of OLCI-B and PRS L_{WN} at 560 nm, (e) OLCI-B versus PRS τ_a at 865 nm, (f) frequency distribution of OLCI-B and PRS α, (g) yearly distribution of OLCI-B τ_a at 865 nm. The continuous and dashed lines in panels (a) and (b) indicate the mean and ± 1 standard deviation, respectively. The error bars associated to *in situ* data indicate measurement uncertainties while those related to satellite data products indicate the variation coefficient determined from the 3×3 elements applied for matchups construction.

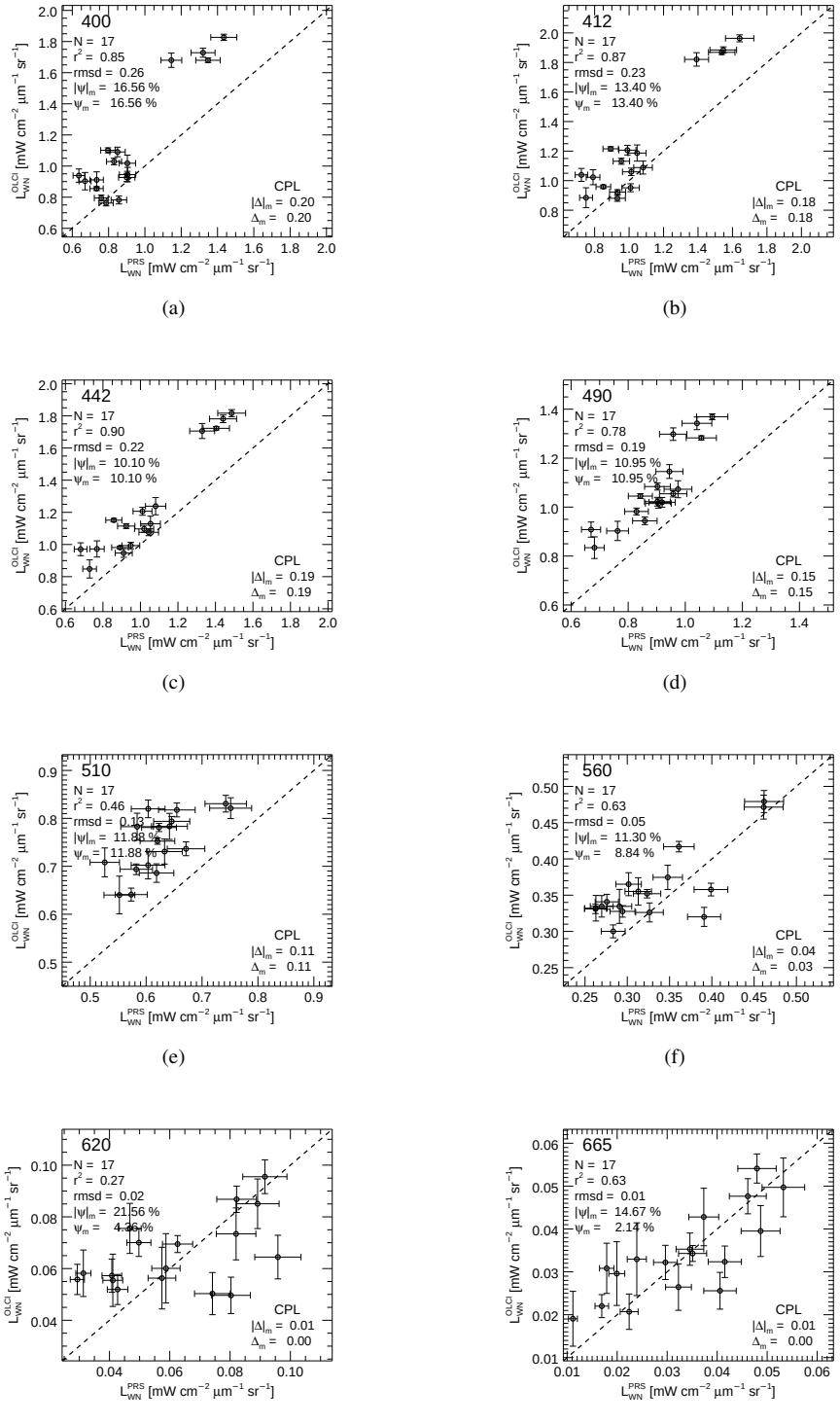

Figure 22: **[S3B@CPL Details]** OLCI-B assessment at the CPL site. Panels display scatter plot of OLCI-B versus PRS L_{WN} aat different center-wavelengths: (a) 400, (b) 412, (c) 442, (d) 490, (e) 510, (f) 560, (g) 620, (h) 665 nm. The error bars associated to *in situ* data indicate measurement uncertainties while those related to satellite data products indicate the variation coefficient determined from the 3×3 elements applied for matchups construction.

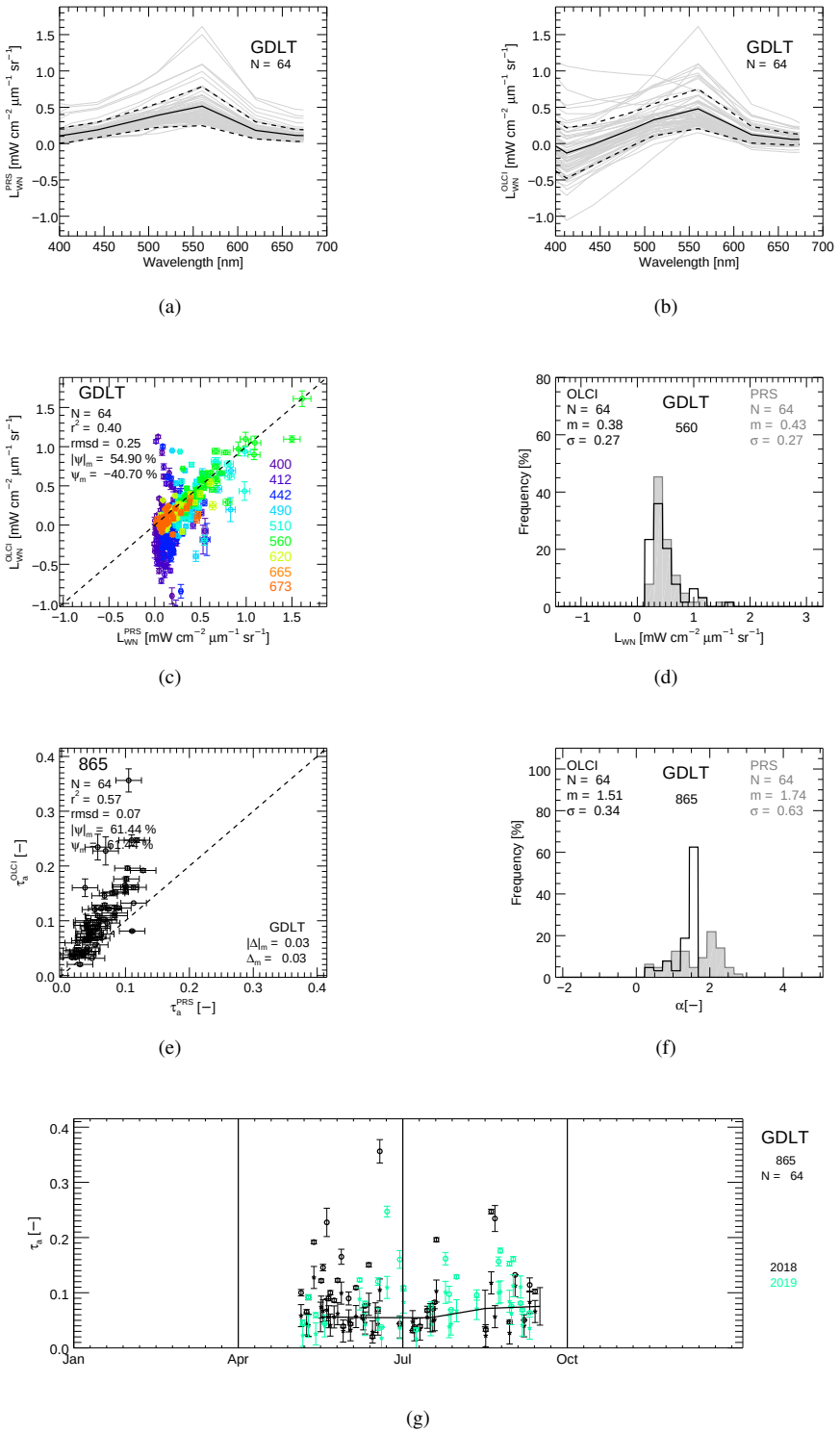

Figure 23: **[S3A@GDLT Overview]** OLCI-A assessment at the GDLT site: (a) PRS L_{WN} spectra, (b) OLCI-A L_{WN} spectra, (c) OLCI-A versus PRS L_{WN} scatter plot, (d) frequency distribution of OLCI-A and PRS L_{WN} at 560 nm, (e) OLCI-A versus PRS τ_a at 865 nm, (f) frequency distribution of OLCI-A and PRS α, (g) yearly distribution of OLCI-A τ_a at 865 nm. The continuous and dashed lines in panels (a) and (b) indicate the mean and ± 1 standard deviation, respectively. The error bars associated to *in situ* data indicate measurement uncertainties while those related to satellite data products indicate the variation coefficient determined from the 3×3 elements applied for matchups construction.

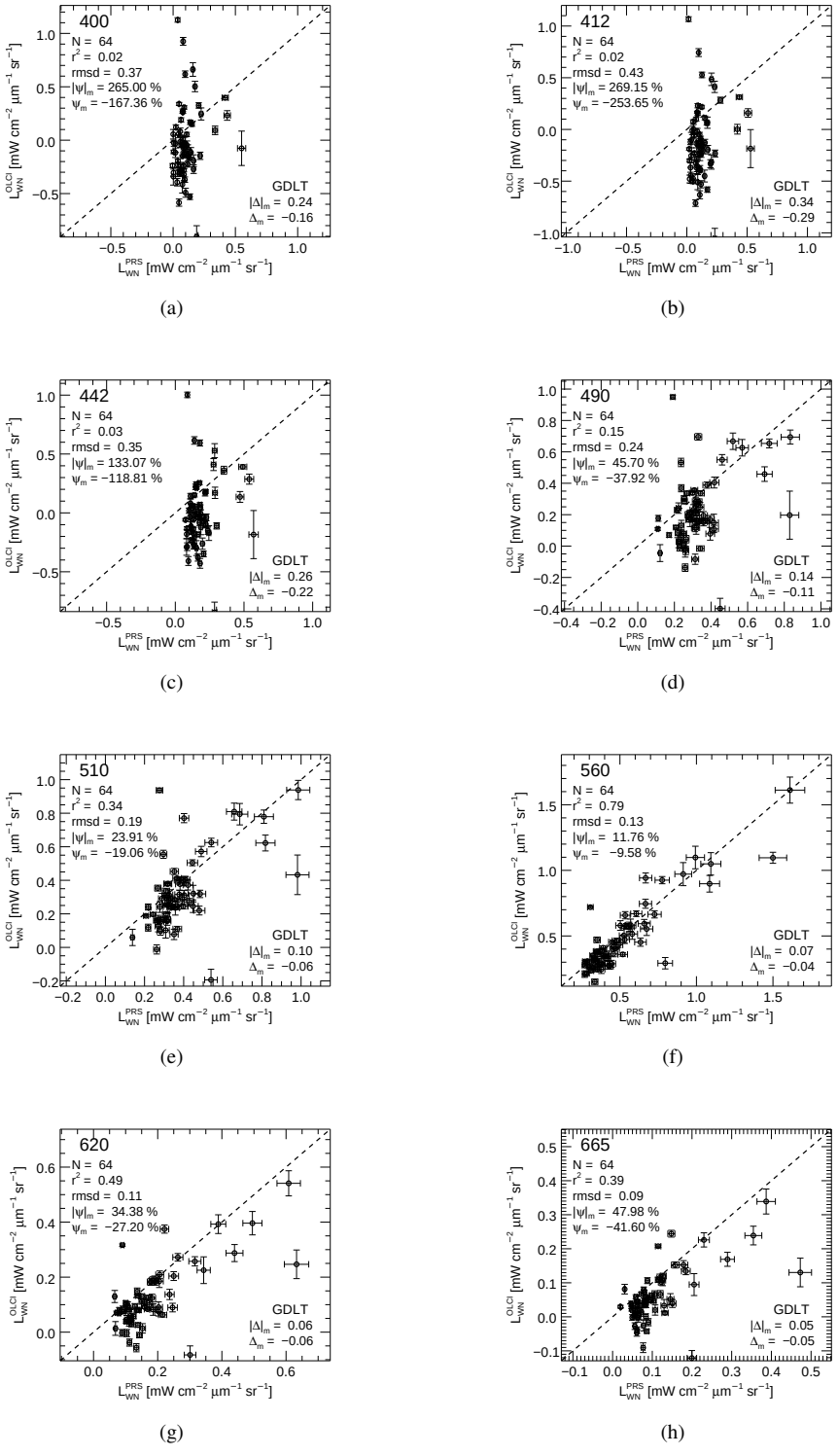

Figure 24: **[S3A@GDLT Details]** OLCI-A assessment at the GDLT site. Panels display scatter plot of OLCI-A versus PRS L_{WN} at different center-wavelengths: (a) 400, (b) 412, (c) 442, (d) 490, (e) 510, (f) 560, (g) 620, (h) 665 nm. The error bars associated to *in situ* data indicate measurement uncertainties while those related to satellite data products indicate the variation coefficient determined from the 3×3 elements applied for matchups construction.

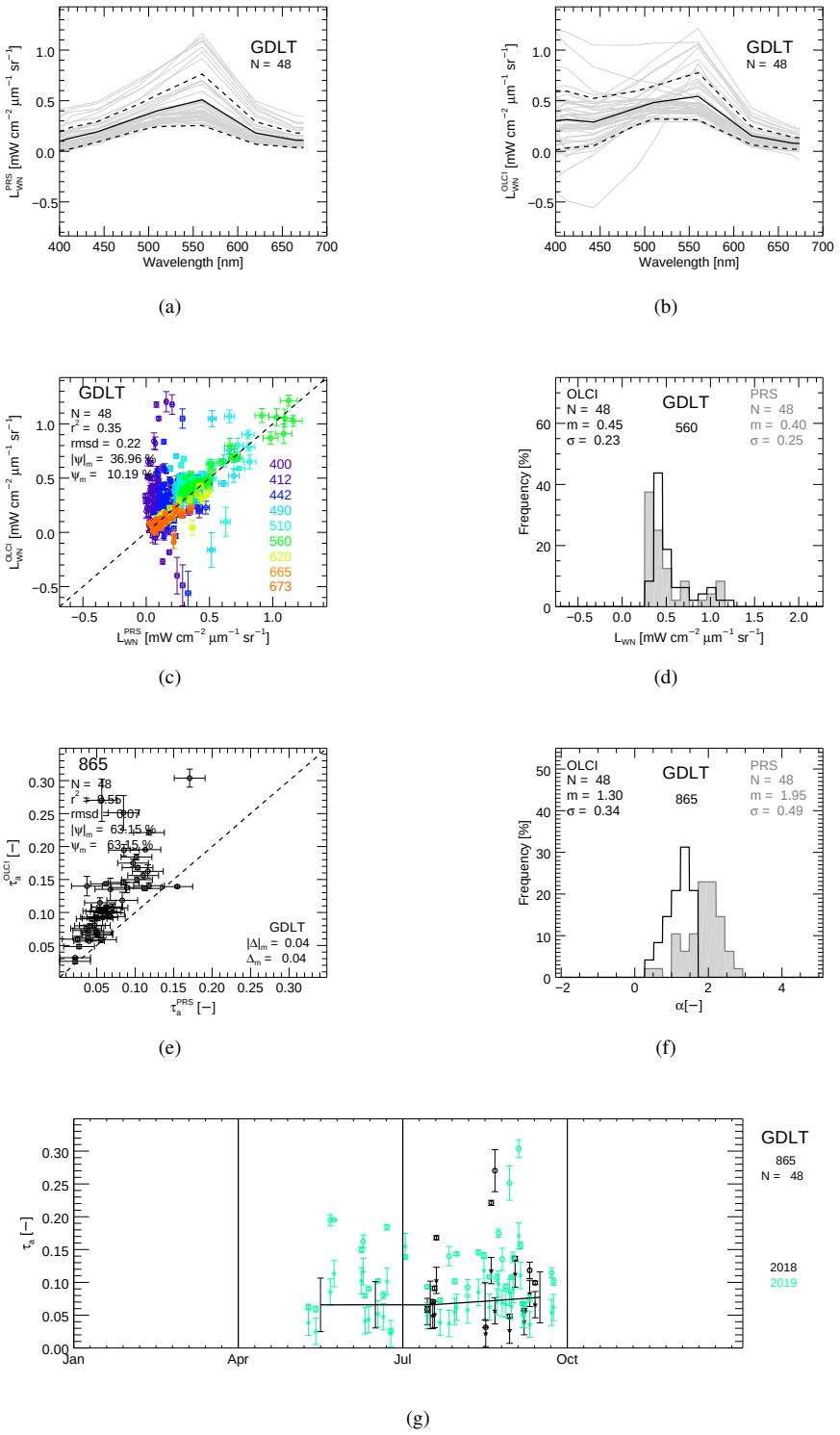

Figure 25: **[S3B@GDLT Overview]** OLCI-B assessment at the GDLT site: (a) PRS L_{WN} spectra, (b) OLCI-B L_{WN} spectra, (c) OLCI-B versus PRS L_{WN} scatter plot, (d) frequency distribution of OLCI-B and PRS L_{WN} at 560 nm, (e) OLCI-B versus PRS τ_a at 865 nm, (f) frequency distribution of OLCI-B and PRS α, (g) yearly distribution of OLCI-B τ_a at 865 nm. The continuous and dashed lines in panels (a) and (b) indicate the mean and ± 1 standard deviation, respectively. The error bars associated to *in situ* data indicate measurement uncertainties while those related to satellite data products indicate the variation coefficient determined from the 3×3 elements applied for matchups construction.

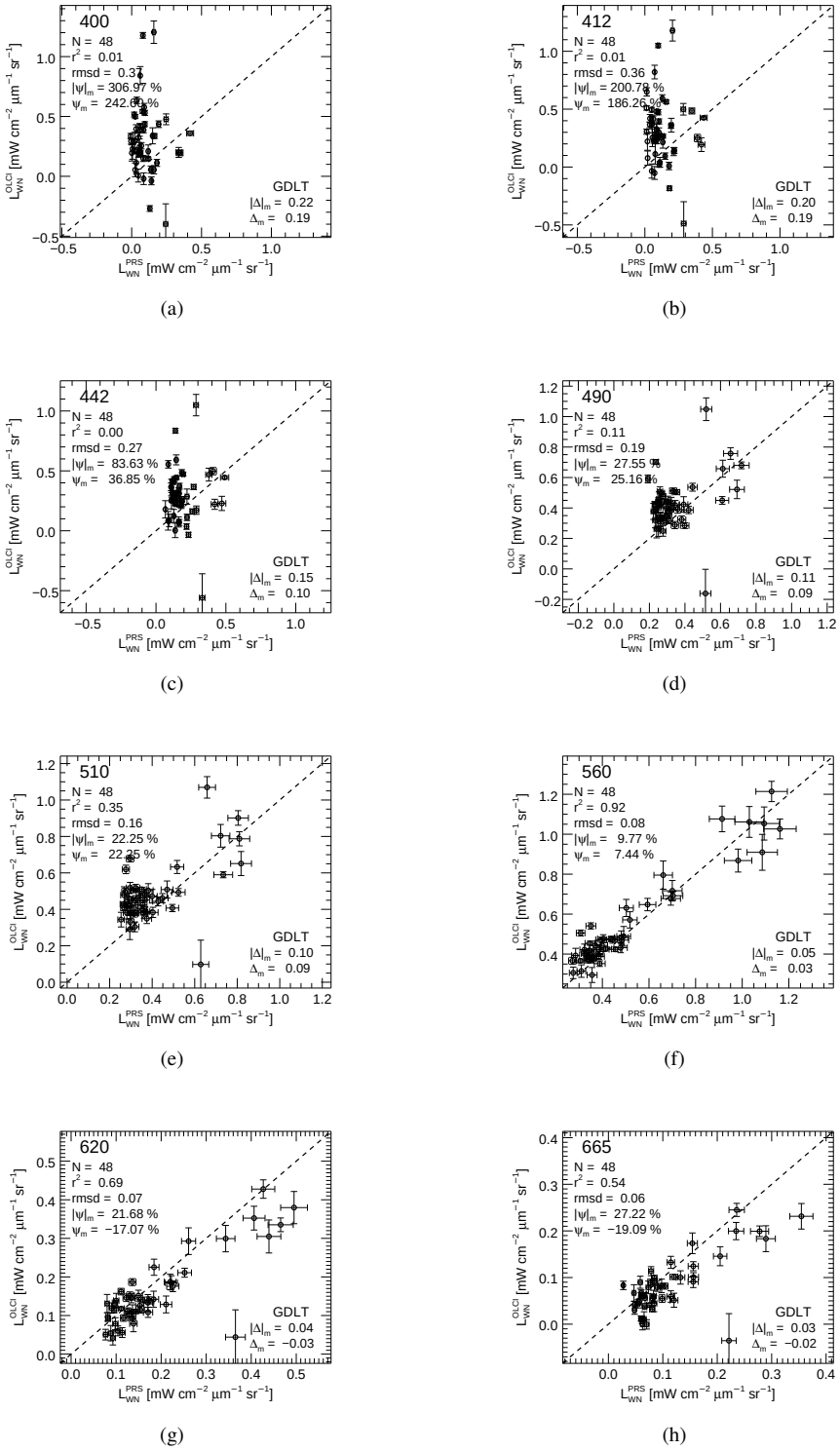

Figure 26: **[S3B@GDLT Details]** OLCI-B assessment at the GDLT site. Panels display scatter plot of OLCI-B versus PRS L_{WN} at different center-wavelengths: (a) 400, (b) 412, (c) 442, (d) 490, (e) 510, (f) 560, (g) 620, (h) 665 nm. The error bars associated to *in situ* data indicate measurement uncertainties while those related to satellite data products indicate the variation coefficient determined from the 3×3 elements applied for matchups construction.

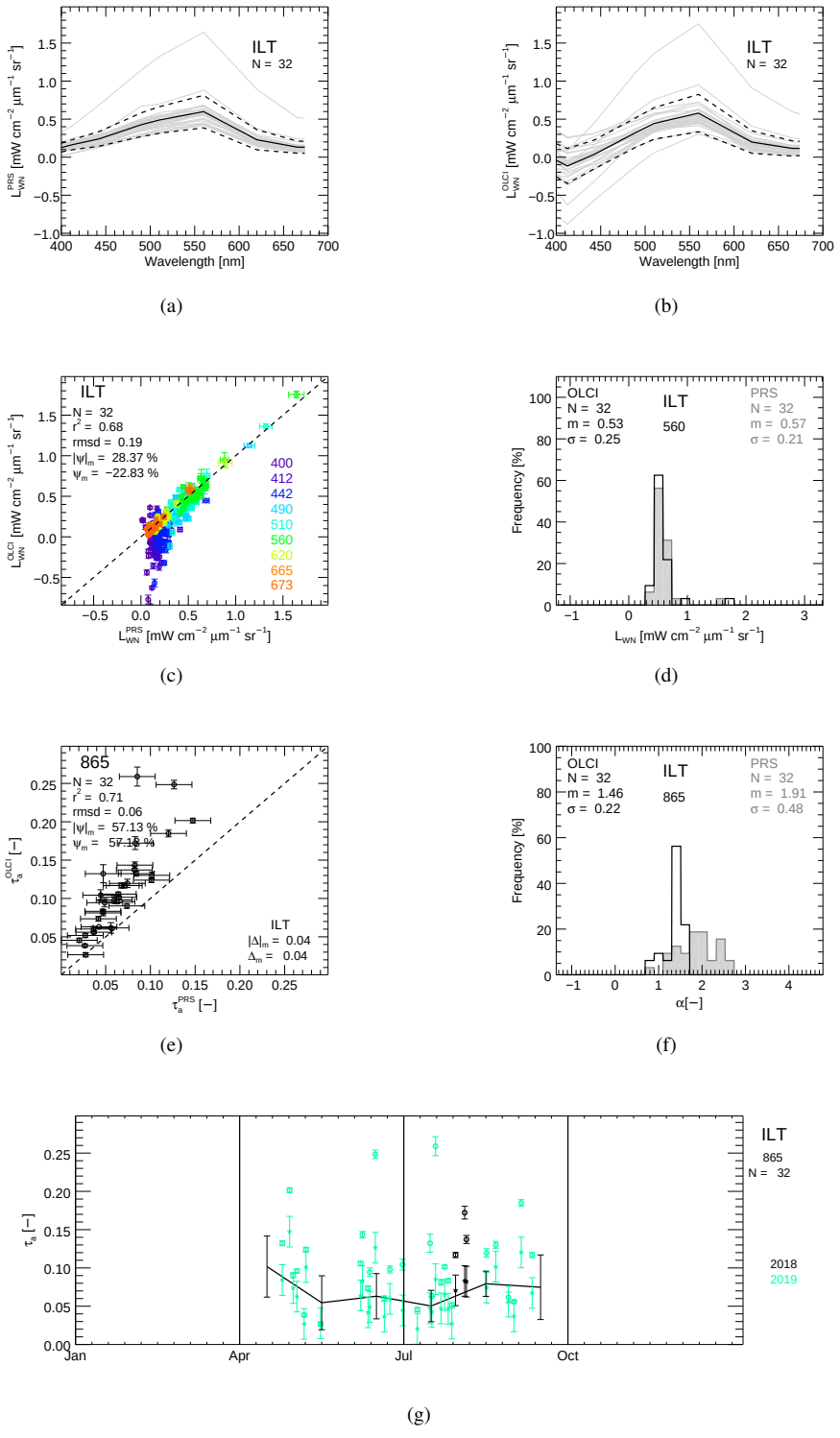

Figure 27: **[S3A@ILT Overview]** OLCI-A assessment at the ILT site: (a) PRS L_{WN} spectra, (b) OLCI-A L_{WN} spectra, (c) OLCI-A versus PRS L_{WN} scatter plot, (d) frequency distribution of OLCI-A and PRS L_{WN} at 560 nm, (e) OLCI-A versus PRS τ_a at 865 nm, (f) frequency distribution of OLCI-A and PRS α, (g) yearly distribution of OLCI-A τ_a at 865 nm. The continuous and dashed lines in panels (a) and (b) indicate the mean and ± 1 standard deviation, respectively. The error bars associated to *in situ* data indicate measurement uncertainties while those related to satellite data products indicate the variation coefficient determined from the 3×3 elements applied for matchups construction.

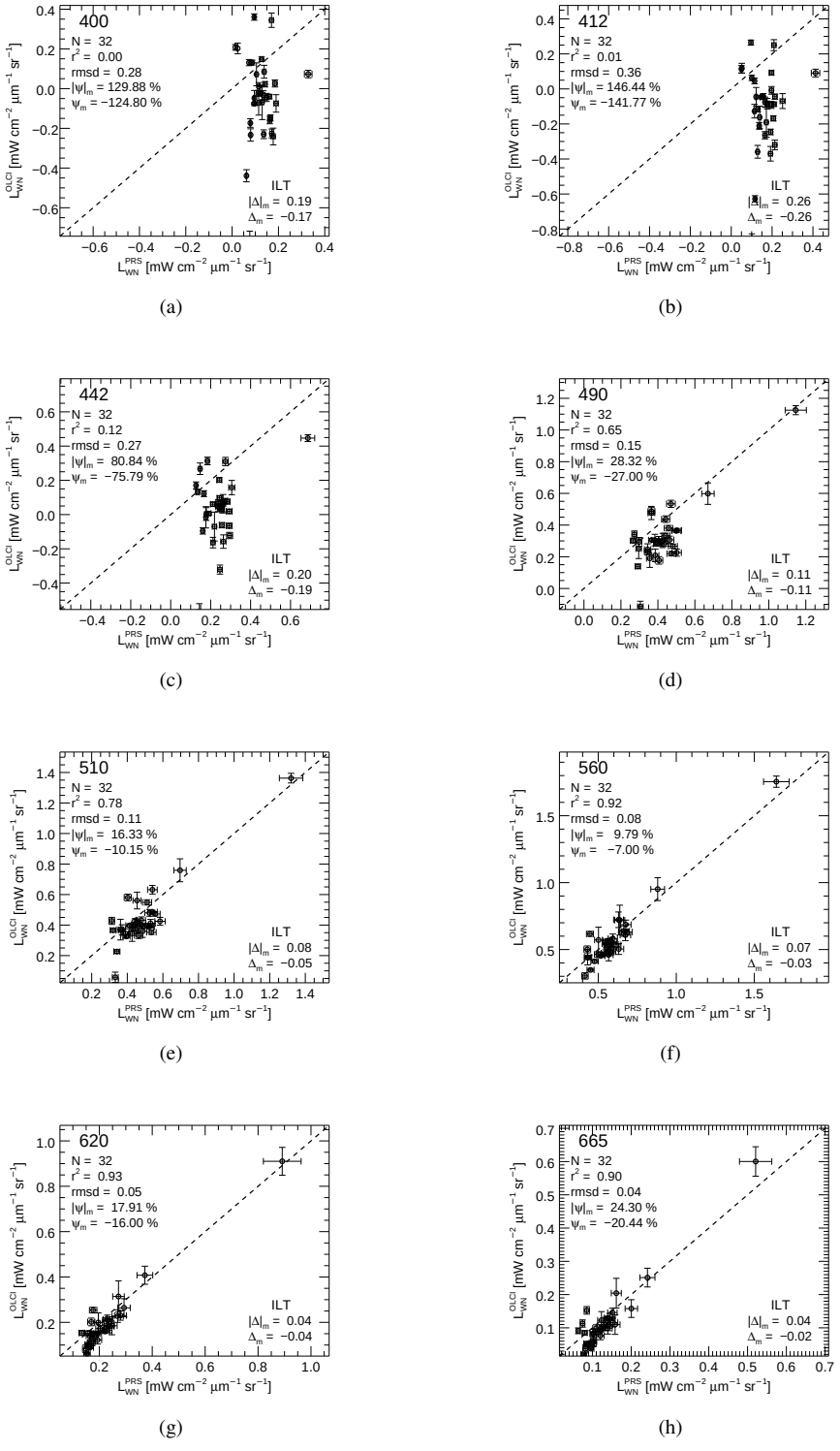

Figure 28: **[S3A@ILT Details]** OLCI-A assessment at the ILT site. Panels display scatter plot of OLCI-A versus PRS L_{WN} at different center-wavelengths: (a) 400, (b) 412, (c) 442, (d) 490, (e) 510, (f) 560, (g) 620, (h) 665 nm. The error bars associated to *in situ* data indicate measurement uncertainties while those related to satellite data products indicate the variation coefficient determined from the 3×3 elements applied for matchups construction.

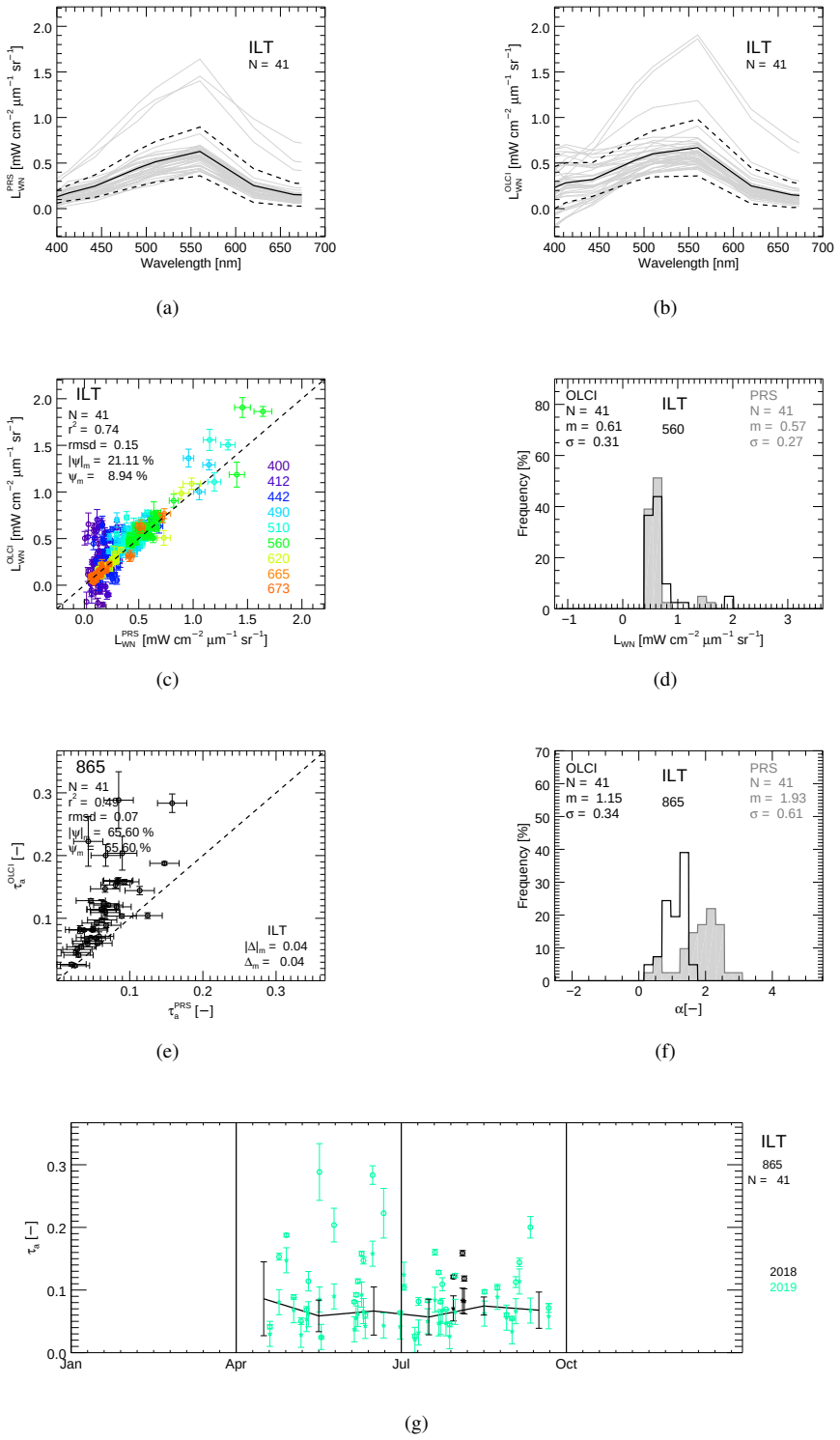

Figure 29: **[S3B@ILT Overview]** OLCI-B assessment at the ILT site: (a) PRS L_{WN} spectra, (b) OLCI-B L_{WN} spectra, (c) OLCI-B versus PRS L_{WN} scatter plot, (d) frequency distribution of OLCI-B and PRS L_{WN} at 560 nm, (e) OLCI-B versus PRS τ_a at 865 nm, (f) frequency distribution of OLCI-B and PRS α, (g) yearly distribution of OLCI-B τ_a at 865 nm. The continuous and dashed lines in panels (a) and (b) indicate the mean and ± 1 standard deviation, respectively. The error bars associated to *in situ* data indicate measurement uncertainties while those related to satellite data products indicate the variation coefficient determined from the 3×3 elements applied for matchups construction.

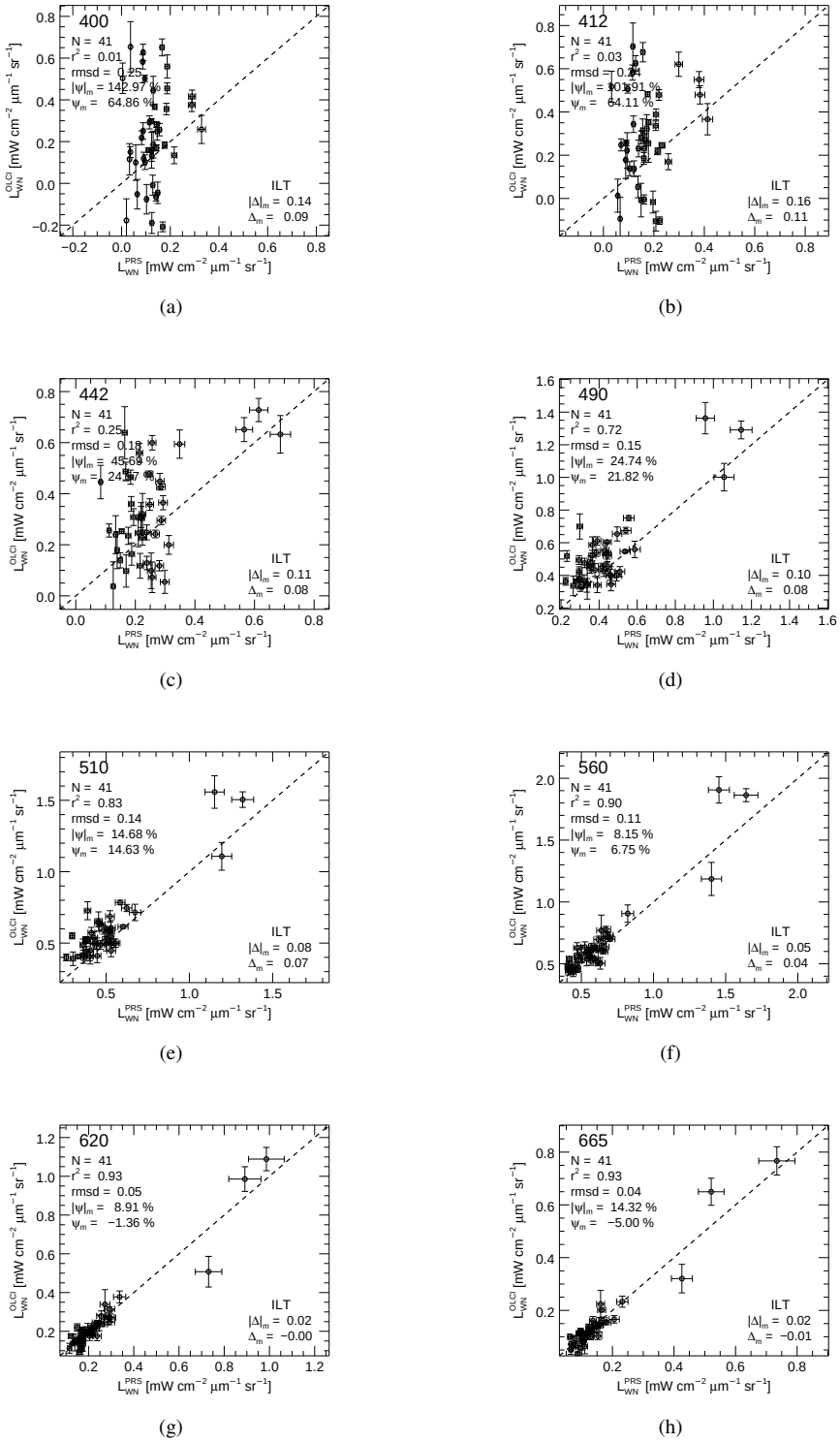

Figure 30: **[S3B@ILT Details]** OLCI-B assessment at the ILT site. Panels display scatter plot of OLCI-B versus PRS L_{WN} at different center-wavelengths: (a) 400, (b) 412, (c) 442, (d) 490, (e) 510, (f) 560, (g) 620, (h) 665 nm. The error bars associated to *in situ* data indicate measurement uncertainties while those related to satellite data products indicate the variation coefficient determined from the 3×3 elements applied for matchups construction.

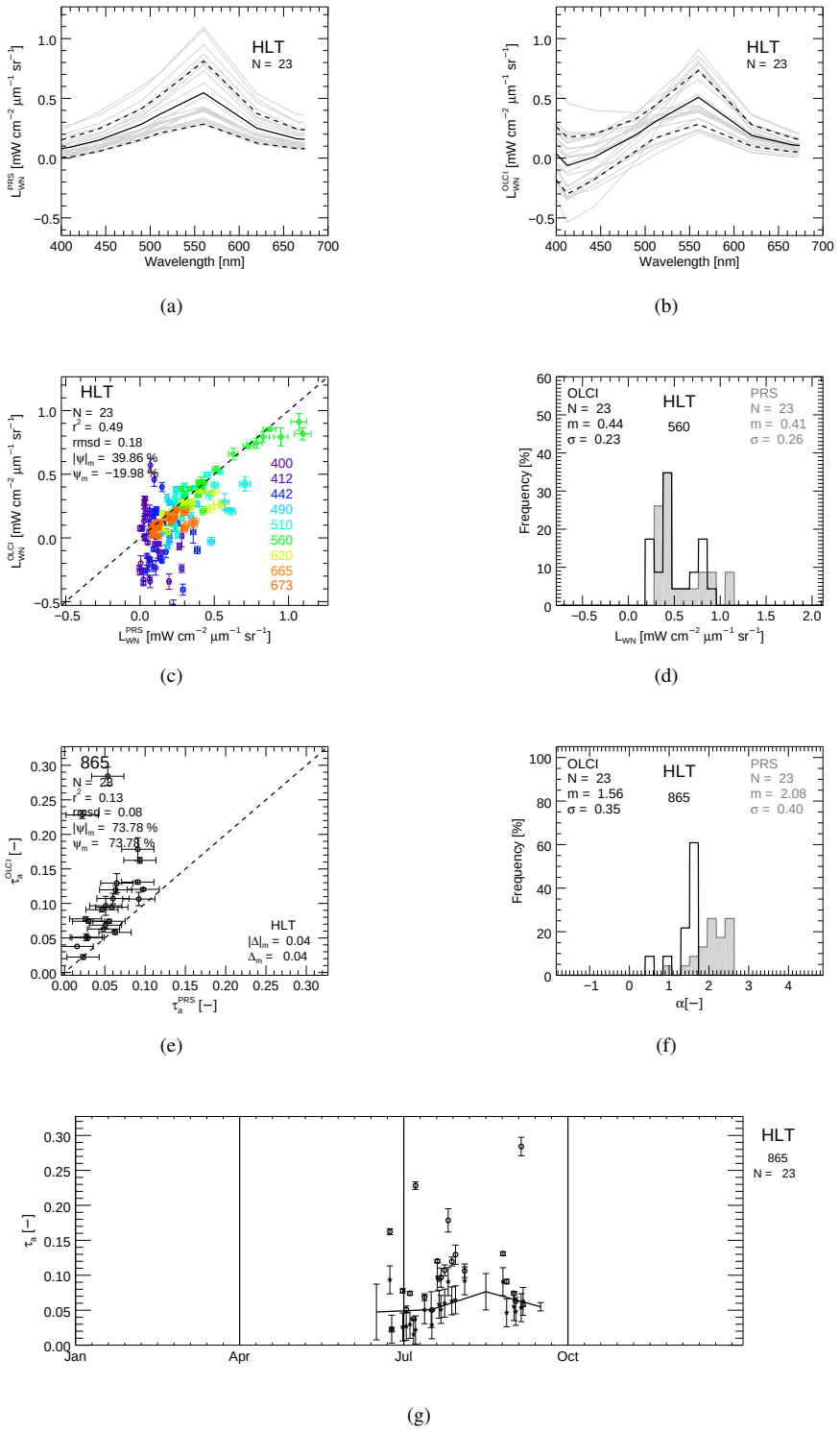

Figure 31: **[S3A@HLT Overview]** OLCI-A assessment at the HLT site: (a) PRS L_{WN} spectra, (b) OLCI-A L_{WN} spectra, (c) OLCI-A versus PRS L_{WN} scatter plot, (d) frequency distribution of OLCI-A and PRS L_{WN} at 560 nm, (e) OLCI-A versus PRS τ_a at 865 nm, (f) frequency distribution of OLCI-A and PRS α, (g) yearly distribution of OLCI-A τ_a at 865 nm. The continuous and dashed lines in panels (a) and (b) indicate the mean and ± 1 standard deviation, respectively. The error bars associated to *in situ* data indicate measurement uncertainties while those related to satellite data products indicate the variation coefficient determined from the 3×3 elements applied for matchups construction.

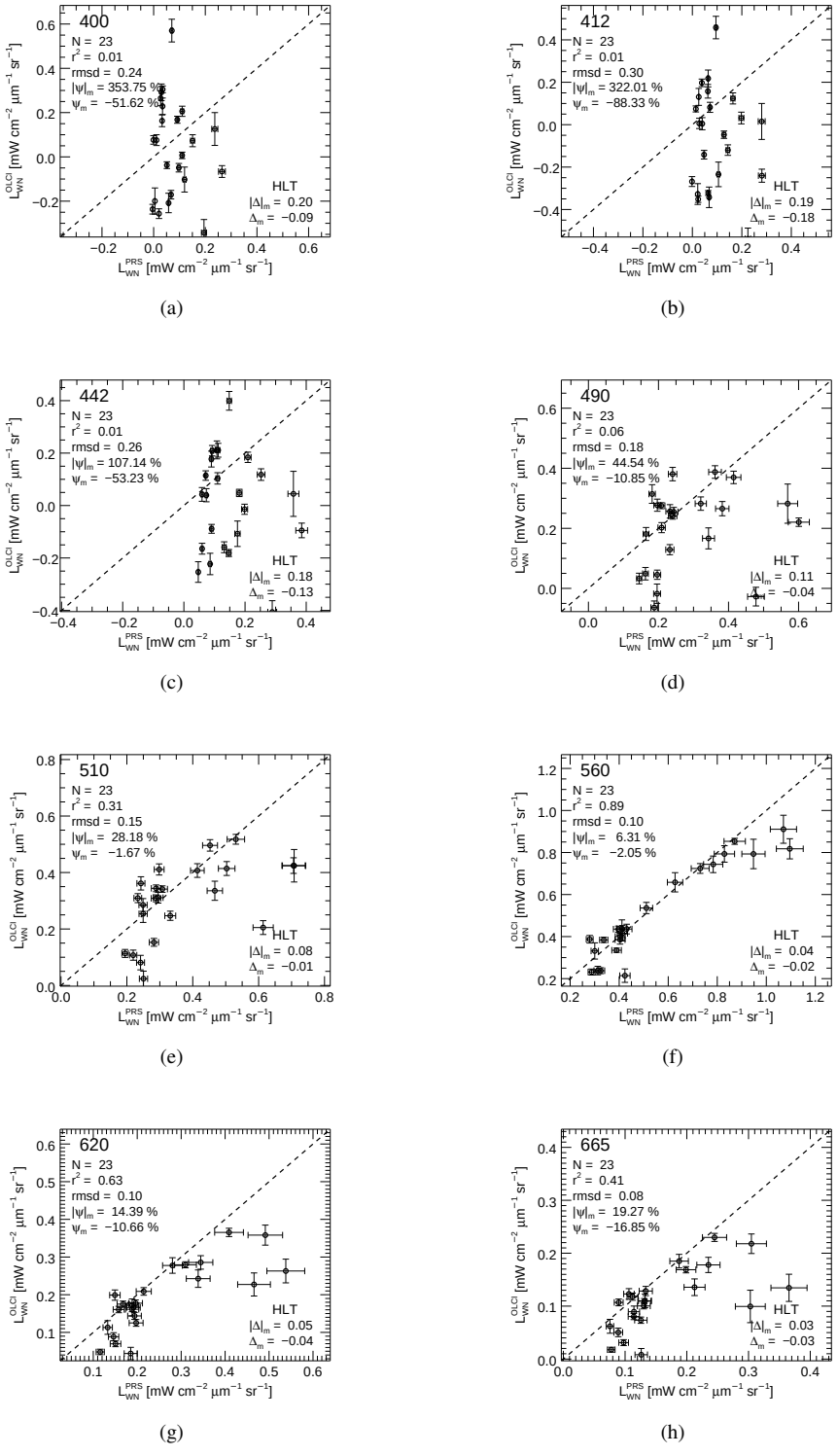

Figure 32: **[S3A@HLT Details]** OLCI-A assessment at the HLT site. Panels display scatter plot of OLCI-A versus PRS L_{WN} at different center-wavelengths: (a) 400, (b) 412, (c) 442, (d) 490, (e) 510, (f) 560, (g) 620, (h) 665 nm. The error bars associated to *in situ* data indicate measurement uncertainties while those related to satellite data products indicate the variation coefficient determined from the 3×3 elements applied for matchups construction.

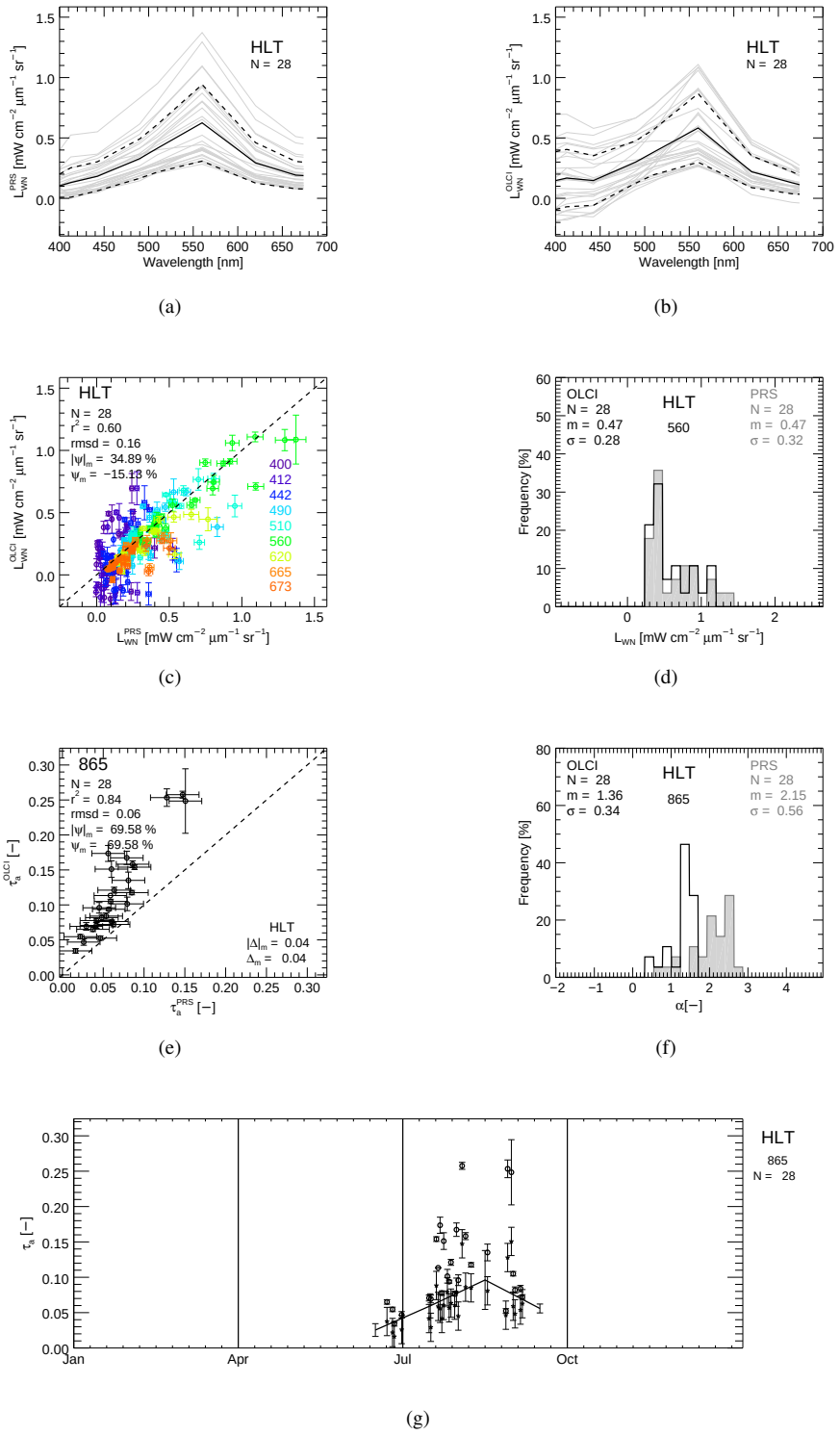

Figure 33: **[S3B@HLTn Overview]** OLCI-B assessment at the HLT site: (a) PRS L_{WN} spectra, (b) OLCI-B L_{WN} spectra, (c) OLCI-B versus PRS L_{WN} scatter plot, (d) frequency distribution of OLCI-B and PRS L_{WN} at 560 nm, (e) OLCI-B versus PRS τ_a at 865 nm, (f) frequency distribution of OLCI-B and PRS α, (g) yearly distribution of OLCI-B τ_a at 865 nm. The continuous and dashed lines in panels (a) and (b) indicate the mean and ± 1 standard deviation, respectively. The error bars associated to *in situ* data indicate measurement uncertainties while those related to satellite data products indicate the variation coefficient determined from the 3×3 elements applied for matchups construction.

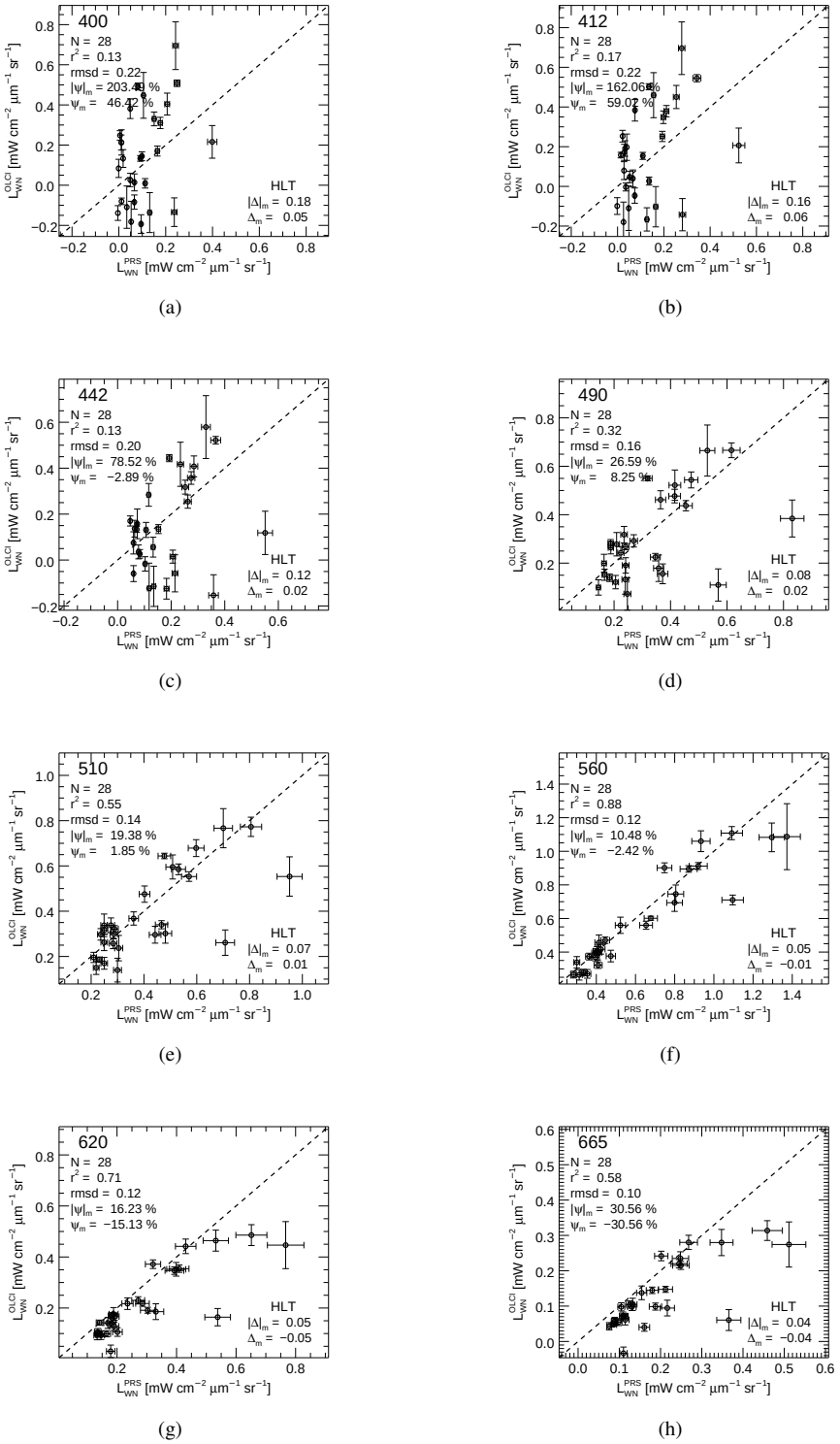

Figure 34: **[S3B@HLT Details]** OLCI-B assessment at the HLT site. Panels display scatter plot of OLCI-B versus PRS L_{WN} at different center-wavelengths: (a) 400, (b) 412, (c) 442, (d) 490, (e) 510, (f) 560, (g) 620, (h) 665 nm. The error bars associated to *in situ* data indicate measurement uncertainties while those related to satellite data products indicate the variation coefficient determined from the 3×3 elements applied for matchups construction.

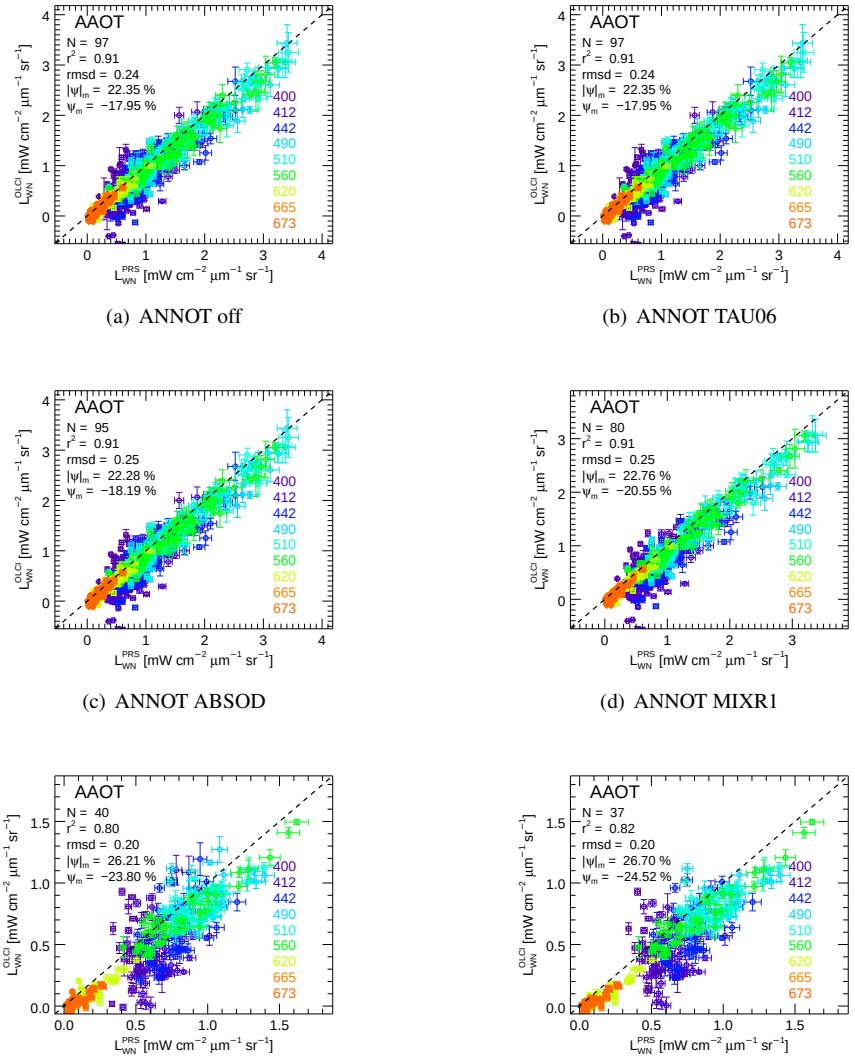

(a) ANNOT off

(b) ANNOT TAU06

(c) ANNOT ABSOD

(d) ANNOT MIXR1

(e) ANNOT DROUT

(f) ANNOT on

Figure 35: **[S3A@AAOT All bands]** ANNOT Flags performance verified for OLCI-A L_{WN} at the AAOT site: (a) ANNOT Flags not applied, (b) ANNOT TAU06 applied, (c) ANNOT ABSDO applied, (d) ANNOT MIXR1 applied, (e) ANNOT DROUT applied, (f) all ANNOT Flags applied. The error bars associated to *in situ* data indicate measurement uncertainties while those related to satellite data products indicate the variation coefficient determined from the 3×3 elements applied for matchups construction.

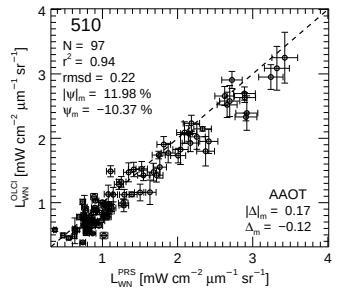

(a) ANNOT off

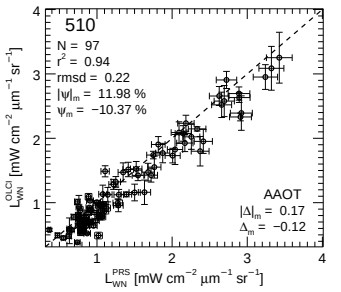

(b) ANNOT TAU06

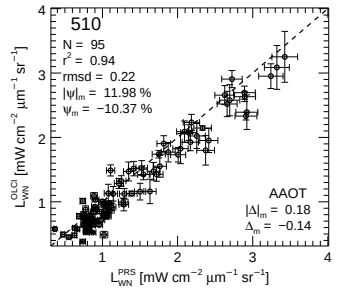

(c) ANNOT ABSOD

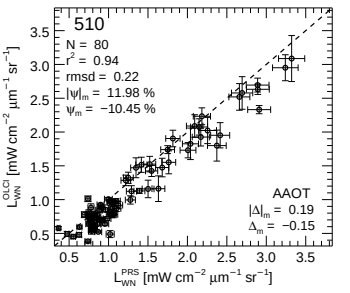

(d) ANNOT MIXR1

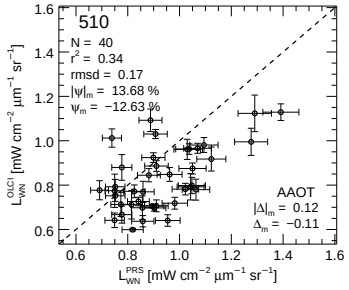

(e) ANNOT DROUT

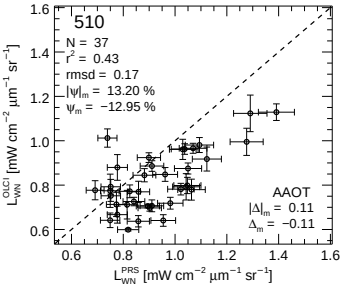

(f) ANNOT on

Figure 36: **[S3A@AAOT Single band]** ANNOT Flags performance verified for OLCI-A $L_{WN}(510)$ at the AAOT site: (a) ANNOT Flags not applied, (b) ANNOT TAU06 applied, (c) ANNOT ABSDO applied, (d) ANNOT MIXR1 applied, (e) ANNOT DROUT applied, (f) all ANNOT Flags applied. The error bars associated to *in situ* data indicate measurement uncertainties while those related to satellite data products indicate the variation coefficient determined from the 3×3 elements applied for matchups construction.

5. Summary and Conclusions

The comparisons between satellite OLCI-A and OLCI-B and *in situ* AERONET-OC normalized water-leaving radiances L_{WN}, indicate a general systematic underestimate of satellite radiometric products for OLCI-A and overestimate for OLCI-B. While both OLCI-A and OLCI-B aerosol optical depths τ_a at 865 nm resulting from the atmospheric correction process indicate systematic overestimates, the derived Ångström exponent α exhibits a very narrow distribution close to a maximum value of approximately 1.7. These findings indicate difficulty in separating water and atmospheric contributions likely explained by: *i.* biases in calibration coefficients that for OLCI-B clearly resulting from the non-application of the System Vicarious Calibration (SVC); or *ii*. the poor performance of the Bright Pixel Correction (BPC) likely affected by an inaccurate determination of aerosol load and type.

Additional finding from this matchups analysis are some spectral inconsistencies affecting both OLCI-A and OLCI-B L_{WN} data in the blue spectral region (particularly evident in the OLCI-A L_{WN} data at 400 nm). Such a result shown by the comparison between satellite and AERONET-OC data from 12-channel systems, can be likely solved through accurate SVC.

References

B. Bulgarelli, V. Kiselev, and G. Zibordi, "Simulation and analysis of adjacency effects in coastal waters: a case study," *Applied Optics, 53*, 1523-1545, 2014

EUMETSAT, "Sentinel-3A Product Notice – OLCI Level-2 Ocean Colour Operational Products and Full-Mission Reprocessed Time Series," Product notice EUM/OPS-SEN3/DOC/17/964713, 2018.

EUMETSAT, "Sentinel-3 OLCI Marine User Handbook," EUM/OPS-SEN3/MAN/17/907205, 2018.

EUMETSAT, "Recommendations for Sentinel-3 OLCI Ocean Colour product validations in comparison with in situ measurements – Matchup Protocols," UM/SEN3/DOC/19/1092968, 2019.

M. Gergely, M. and G. Zibordi, "Assessment of AERONET-OC L_{WN} uncertainties," Metrologia, 51, 40–47, 2014.

B. N. Holben, T. F. Eck, I. Slutsker, D. Tanré, J. P. Buis, A. Setzer, E. Vermote, J. A. Reagan, Y. J. Kaufman, T. Nakajima, F. Lavenu, I. Jankowiak and A. Smirnov "AERONET—A federated instrument network and data archive for aerosol characterization," *Remote Sens. Environ.*, **66**, 1–16, 1998.

B. N. Holben, D. Tanre, A. Smirnov A., T. F. Eck I. Slutsker I., N. Abuhassan, W. W. Newcomb, J. Schafer, B. Chatenet, F. Lavenue, Y. J. Kaufman, J. Vande Castle, A. Setzer, B. Markham, D. Clark, R. Frouin, R. Halthore, A. Karnieli, N.T. O'Neill, C. Pietras, R. T. Pinker, K. Voss and G. Zibordi."An emerging ground-based aerosol climatology: Aerosol Optical Depth from AERONET," *J. Geophys. Res.*, **106**, 12067–12097, 2001

F. Mélin, G. Zibordi, T. Carlund, B. N. Holben, and S. Stefan, "Validation of SeaWiFS and MODIS Aqua/Terra aerosol products in coastal regions of European marginal seas," *Oceanologia*, 55, 27–51, 2013.

G. Thuillier, M. Hersé, D. Labs, T. Foujols, W. Peetermans, Gillotay, P.C. Simon, and H. Mandel, "The solar spectral irradiance from 200 to 2400 nm as measured by the SOLSPEC spectrometer from the Atlas and Eureca missions," *Solar Phys*ics 214, 1–22, 2003.

G. Zibordi, J. F. Berthon, F. Mélin, D. D'Alimonte, and S. Kaitala, "Validation of satellite ocean colour primary products at optically complex coastal sites: Northern Adriatic Sea, Northern Baltic Proper and Gulf of Finland," *Remote Sensing of Environment*, 113, 2574-2591, 2009b.

G. Zibordi, F. Mélin, J.-F. Berthon, "A regional assessment of OLCI data products," *IEEE Geoscience and Remote Sensing Letters*, 15, 1490–1494, 2018.

G. Zibordi, F. Mélin, J.-F. Berthon, and E. Canuti, "Assessment of MERIS ocean color data products for European seas," *Ocean Sci*, 9, pp. 521–533, 2013.

G. Zibordi, B. Holben, I. Slutsker, D. Giles, D. D'Alimonte, F. Melín, J.-F. Berthon, D. Vandemark, H. Feng, G. E. Schuster, B. Fabbri, S. Kaitala, and J. Seppala, "AERONET-OC: a network for validation of ocean color primary products," J. Atmospheric Ocean. Technol. **26**, 1634–1651 (2009).

List of acronyms

AAOT	Acqua Alta Oceanographic Tower
AERONET	Aerosol Robotic Network
AERONET-OC	Ocean Colour component of the Aerosol Robotic Network
BPC	Bright Pixel Correction
CDOM	Coloured Dissolved Organic Matter
CODAREP	Copernicus Online Data Access Reprocessed
CPL	Casablanca Platform
DG-GROW	Directorate General for Internal Market, Industry Entrepreneurship and SMEs
DG-JRC	Directorate General - Joint Research Centre
EOSS	Earth Observation Support to Copernicus Climate and Marine Services
EUMETSAT	European Organization for the Exploitation of Meteorological Satellites
FR	Full Resolution
GDLT	Gustaf Dalen Lighthouse Tower
GLR	Gloria Platform
GLT	Galata Platform
GSFC	Goddard Space Flight Center
HLT	Helsinki Lighthouse Tower
ILT	Irbe Lighthouse Tower
LAC	Local Acquisition Area
MERIS	MEdium Resolution Imaging Spectrometer
MODIS	Medium Resolution Imaging Spectrometer
NASA	National Aeronautics and Space Administration
NPP	National Polar-Orbiting Partnership
NTC	Non Critical Time
OLCI	Ocean and Land Colour Instrument
OLCI-A	OLCI on-board Sentinel 3A
OLCI-B	OLCI on-board Sentinel 3B
RR	Reduced Resolution
SeaPRISM	SeaWiFS Photometer Revision for Incident Surface Measurements
SeaWiFS	Sea-viewing Wide Field-of-View Sensor
ST-7	Station-7 Platform
SVC	System Vicarious Calibration
VIIRS	Visible Infrared Imaging Radiometer Suite

GETTING IN TOUCH WITH THE EU

In person

All over the European Union there are hundreds of Europe Direct information centres. You can find the address of the centre nearest you at: https://europa.eu/european-union/contact_en

On the phone or by email

Europe Direct is a service that answers your questions about the European Union. You can contact this service:

- by freephone: 00 800 6 7 8 9 10 11 (certain operators may charge for these calls),

- at the following standard number: +32 22999696, or

- by electronic mail via: https://europa.eu/european-union/contact_en

FINDING INFORMATION ABOUT THE EU

Online

Information about the European Union in all the official languages of the EU is available on the Europa website at: https://europa.eu/european-union/index_en

EU publications

You can download or order free and priced EU publications from EU Bookshop at: https://publications.europa.eu/en/publications. Multiple copies of free publications may be obtained by contacting Europe Direct or your local information centre (see https://europa.eu/european-union/contact_en).

KJ-NA-29973-EN-N

The European Commission's science and knowledge service

Joint Research Centre

JRC Mission

As the science and knowledge service of the European Commission, the Joint Research Centre's mission is to support EU policies with independent evidence throughout the whole policy cycle.

EU Science Hub

ec.europa.eu/jrc

@EU_ScienceHub

EU Science Hub - Joint Research Centre

EU Science, Research and Innovation

EU Science Hub

Publications Office of the European Union

doi:10.2760/41229

ISBN 978-92-76-13039-0